Strong Sensitivity of Simulated Supercells to Low-Level Moisture: Effects of Near-Cloud-Base Moisture Entrainment

JINLIN LI[a] AND MING XUE[b]

[a] *Key Laboratory of Mesoscale Severe Weather, Ministry of Education, School of Atmospheric Sciences, Nanjing University, Nanjing, Jiangsu, China*

[b] *Center for Analysis and Prediction of Storms and School of Meteorology, University of Oklahoma, Norman, Oklahoma*

(Manuscript received 10 December 2024, in final form 5 November 2025, accepted 12 December 2025)

ABSTRACT: Idealized numerical simulations using a climatological composite sounding of significant tornadoes within China failed to produce a sustained storm. An increase in vertical wind shear showed minimal impact on storm longevity. The simulated storms exhibited very high sensitivity to environmental humidity near the cloud base, at 1–2 km above ground. Increasing humidity within this layer led to the formation of long-lived (≥2 h) and more intense supercells, even though the increase did not change much standard environmental parameters including the lifting condensation level (LCL) and convective available potential energy (CAPE). LCL and CAPE are important environmental parameters that are components of the significant tornado parameter (STP) used in tornado forecasting operations. This strong sensitivity is investigated. Instead of calculating airmass fluxes, water vapor entrainment into storms is calculated as moisture fluxes across the interface between the storm updraft core and its surrounding environment, which also includes that at the cloud base. Results show that more environmental moisture is entrained into the updraft core of simulated storms when the humidity in the 1–2-km layer AGL is increased. The resulting greater positive buoyancy due to the release of more latent heat leads to larger vertical acceleration and steeper slopes of the air parcel trajectories and, therefore, more upright updrafts. The generation of positive inflow shear due to the enhanced near-surface inflow further increases the uprightness of updraft at the lower levels. As a result, the convective cells stay close to the low-level gust fronts, and intense supercell storms are sustained throughout the 2-h simulation.

SIGNIFICANCE STATEMENT: This study demonstrates that increasing relative humidity solely within the 1–2-km layer above ground level in a sounding based on the composite environment of significant tornadoes in China transforms simulated supercells from short-lived to intense and long-lasting ones, despite minimal changes to environmental parameters such as convective available potential energy (CAPE) and lifting condensation level (LCL). The enhanced humidity leads to increased entrainment of environmental moisture into the storm updraft near the cloud base, and substantially larger updraft buoyancy and intensity. As a result, the updrafts become more upright and remain close to the low-level gust front, and the strong storms are sustained for longer durations. These findings highlight the critical role of water vapor entrainment near cloud base in governing simulated supercell longevity and intensity, an aspect not previously investigated in detail.

KEYWORDS: Clouds; Mesoscale processes; Water vapor; Operational forecasting; Cloud resolving models

1. Introduction

Supercell thunderstorms are responsible for the majority of intense tornadoes (Burgess 1976), with long-lived supercells demonstrating greater tornadic intensity potential compared to their short-lived counterparts (Bunkers et al. 2006). Understanding how the environment influences the longevity and intensity of supercells is, therefore, of critical importance.

Environmental conditions and associated parameters, such as vertical wind shear, convective available potential energy (CAPE), storm-relative helicity (SRH), lifting condensation level (LCL), and low-level water vapor, have been shown to significantly influence the mode, intensity, and longevity of both real and simulated supercells (e.g., Weisman and Klemp 1982; Droegemeier et al. 1993; Gilmore and Wicker 1998; McCaul and Cohen 2002). Bulk wind shear, CAPE, SRH, and LCL are all components of the significant tornado parameter (STP; Thompson et al. 2003, 2004), which is operationally used for predicting tornadic potential of thunderstorms developing in the given environment. However, our findings indicate that the supercell's evolution is also sensitive to fine-scale variations that are not adequately captured by the above parameters.

Composite environmental soundings of significant tornado (SIGTOR) represent a form of mean environment based on which idealized simulation studies can be performed (e.g., Parker 2014; Coffer and Parker 2017), including examining the sensitivity of the simulated storms to environmental properties. In the initial phase of this study, a composite sounding associated with SIGTOR in China, as reported by Zhang et al. (2023),

Corresponding author: Ming Xue, mxue@ou.edu

DOI: 10.1175/JAS-D-24-0272.1

was used to define the environment of idealized storm simulations. The fixed STP (STPfix; Coffer et al. 2019) of this composite sounding is 0.65, which represents a relatively high value within the Chinese region for tornado potential (Zhang et al. 2025). Nevertheless, the simulations failed to produce sustained convective storms beyond 1 h (see section 3a). The relatively weak vertical wind shear, compared to that observed in U.S. tornado cases (Zhou et al. 2022; Zhang et al. 2023), was suspected to be a key factor limiting the longevity of the simulated storms.[1] In general, environments characterized by strong wind shear are more conducive to long-lasting convective storms (Weisman and Klemp 1982, 1984, 1986; Rotunno et al. 1988; Weisman and Rotunno 2000; Bunkers et al. 2006), although recent studies also pointed out that stronger shear can suppress the initial development of the storms due to enhanced mixing with the storm environment (Peters et al. 2022a,b).

In our study, enhancing vertical wind shear did not promote the storm longevity, however (see section 3b). Instead, we found that the simulated storms, including their mode, intensity, and particularly longevity, were highly sensitive to variations in low-level environmental moisture, especially that near the boundary layer top and cloud base. The simulated storms—particularly the right-moving supercell that emerges following storm splitting—become stronger and long-lasting when the relative humidity (RH) in the 1–2-km layer AGL is increased (up to 94%, see section 3c), even though this modification has negligible effects on environmental parameters such as CAPE and LCL. This prompts us to ask the questions: Why does environmental humidity within this thin layer have such a large impact on the simulated storms, and what are the underlying mechanisms that drive such an impact? These become the primary questions we seek to answer in this study.

Compared to vertical wind shear, the relationship between environmental humidity and supercell storm longevity is comparatively underinvestigated in existing studies. Using idealized simulations with a 1-km grid spacing and a warm-rain microphysics scheme, Gilmore and Wicker (1998) suggested that midtroposphere RH strongly influences supercell longevity and evolution. Their study found that supercells forming in environments with moderate wind shear and very dry midtroposphere typically produce strong low-level outflow that propagates faster than the midlevel mesocyclone, cutting off warm and moist low-level inflow and leading to the demise of supercells after the initial hour of simulation. Increasing the wind shear or positioning the dry air at a higher altitude can mitigate the negative effects of excessively strong low-level outflow.

Through numerical simulations using an ice microphysics scheme with a 250-m grid spacing, James and Markowski (2010) found that dry air in the 2.5–4-km layer (above cloud base) can reduce supercell intensity by promoting entrainment of drier environmental air into the updraft, thereby decreasing the likelihood of a mixed parcel attaining positive buoyancy. Dry air aloft was found to be responsible for the reduction of total condensation, total rainfall, and total mass of each condensate species. In contrast to Gilmore and Wicker (1998), James and Markowski (2010) observed that introducing a dry midtropospheric layer did not enhance the low-level outflow; instead, it led to a weaker cold pool. In simulations with drier environments, weaker updrafts and reduced precipitation, along with the corresponding decrease in melting and evaporative cooling, were found to outweigh the potentially favorable effects of dry air on evaporative cooling. When the simulation in James and Markowski (2010) was rerun using a warm-rain microphysics scheme, the results closely resembled those of Gilmore and Wicker (1998), indicating that the inclusion of ice processes can change the simulation results qualitatively.

Moreover, Grant and van den Heever (2014) conducted a comprehensive investigation into the sensitivity of supercell morphology to the vertical distribution of environmental moisture. Their results demonstrated that supercells became narrower and weaker and produced less precipitation in the presence of dry layers, particularly when those layers were situated at lower altitudes. The entrainment of dry air into the updraft reduced the available water vapor for hydrometeor growth, a finding consistent with that of James and Markowski (2010). Although storm longevity was not the primary focus of their study, we noted that convection in their simulations was poorly maintained when the lowest moisture layer (1.5–2.5 km AGL) was dry, whereas storms were better sustained when dryness was confined to higher altitudes. Importantly, storms failed to maintain in simulations where the dry layer extended marginally into the mixed layer (i.e., their L50 and L25 experiments), likely due to a 10%–20% reduction in mixed-layer CAPE, despite minimal changes in surface-based and most unstable CAPE.

Entrainment, a fundamental process modulating storm evolution, is influenced by environmental humidity. Previous studies, including Raymond and Blyth (1986), Kain and Fritsch (1990), and Brown and Zhang (1997), suggest that entrainment rates generally increase with higher environmental humidity; however, these studies did not directly quantify entrainment rates. Romps (2010) and Dawe and Austin (2011a) proposed two methods to calculate the entrainment of environmental air (in terms of airmass flux rather than moisture flux) into clouds directly, which have been widely adopted in subsequent studies (e.g., Dawe and Austin 2011b; Moser and Lasher-Trapp 2017; Savre 2022).

Jo and Lasher-Trapp (2023, hereafter JLT23) used the method of Dawe and Austin (2011a) to examine how environmental humidity influences precipitation efficiency in simulated supercells via entrainment. They found that the reduction of updraft intensity in terms of the vertical mass flux and the amount of precipitation in supercells within an environment with lower humidity between 3 and 4 km AGL were attributed to the storm-relative airstream entraining less humid low-level air into the storm core.

[1] Because the composite sounding is an average of many soundings representing possibly quite different tornado environments and also there are inaccuracies associated with sounding profiles derived from reanalysis data, the vertical shear in the composite is most likely weaker than that of many individual cases. The same averaging process can also lead to smoother temperature and moisture sounding profiles and drier RH near the cloud base than that of many individual soundings. Future studies can explore composite averages of subgroups of SIGTOR soundings classified according to their similarity.

In an earlier study, Lasher-Trapp et al. (2021, hereafter LT21) identified three primary entrainment mechanisms in idealized supercell thunderstorms: overturning "ribbons," "disorganized turbulent eddies," and the "storm-relative airstream." Of these, the storm-relative airstream refers to warm, moist air streaming into the storm at low altitudes (below ~4 km AGL), which can contribute to latent heat release and precipitation formation. Thus, increased entrainment through the storm-relative airstream, facilitated by higher low-level environmental humidity, can promote storm development.

In a related line of inquiry, Morrison et al. (2022) employed an implied fractional entrainment rate—calculated using bulk methods—to systematically investigate how variations in free-tropospheric environmental relative humidity and updraft radius influence convection initiation, through idealized large-eddy simulations. Their results showed that higher environmental RH allows shallow cumulus to grow into deep convection with a smaller required updraft radius. Additionally, the implied fractional entrainment rate was found to decrease with increasing updraft radius but exhibited limited sensitivity to environmental humidity. Consistent with previous studies (e.g., James and Markowski 2010; JLT23), buoyancy dilution increased with decreasing environmental humidity.

We note that the methods employed, either in Dawe and Austin (2011a) or Romps (2010), directly calculate the entrainment of total air mass rather than the entrainment of water vapor specifically. In those cases, the entrainment of water vapor is only considered implicitly based on the assumption that the entrained environmental air is drier. We believe it is more appropriate to explicitly calculate the entrainment/detrainment of moisture into/out of storms in terms of moisture fluxes. Accordingly, this study investigates the relationship between environmental humidity and deep convection by calculating "water vapor entrainment," which quantifies the amount of moisture entrained/detrained into/out of the updraft cores. Increased moisture entrainment should lead to greater latent heat release upon condensation, thereby enhancing buoyancy and storm intensity, and vice versa.

Few studies have examined the relationship between environmental humidity and simulated storm longevity. Moreover, there remains a general scarcity of research into the mechanisms through which environmental humidity—particularly below 2 km—affects storm evolution, as most previous studies focus on layers above 2 km (e.g., Gilmore and Wicker 1998; James and Markowski 2010; JLT23). Additionally, many prior related studies employed horizontal grid spacings of 250 m or greater, resolutions too coarse to adequately resolve large turbulent eddies that are directly responsible for entrainment and detrainment processes. Furthermore, many of these earlier studies utilized the analytic thermodynamic sounding of Weisman and Klemp (1982).

In this study, we conduct a series of high-resolution numerical experiments based on the SIGTOR composite sounding in China, using a horizontal grid spacing of 100 m. Our primary objective is to investigate how near-cloud-base environmental humidity influences the intensity and longevity of simulated supercell storms, as well as the underlying mechanisms. To this end, we carry out sensitivity experiments by modifying the environmental humidity in specific layers—namely, 1–2, 2–3, and 1–3 km AGL—relative to the control simulation. Entrainment of water vapor into storms is calculated as moisture fluxes across the interface between the storm updraft core and its surrounding environment using a newly developed method, and the impact of entrainment on the simulated storm intensity and longevity is investigated. The effects of environmental moisture entrainment on air parcel buoyancy, updraft vertical velocity, and updraft slope are examined to clarify the governing processes. While this study was initially motivated by efforts to obtain sustained supercell simulations based on the SIGTOR composite sounding for China, the results of sensitivity experiments are broadly applicable beyond the Chinese region.

The rest of this paper is organized as follows. Section 2 describes the simulation configurations, soundings utilized, and the method for calculating water vapor entrainment into the storms. Section 3 discusses the simulation results, and section 4 presents summary and conclusions.

2. Methods

a. Model configurations

The nonhydrostatic Advanced Regional Prediction System (ARPS) (Xue et al. 2000; Xue et al. 2001) is used in this study for generating a series of idealized simulations. The simulation domain is 90 km × 90 km in the horizontal and 16 km in the vertical. Horizontal grid spacing is 100 m. There are 83 vertical levels, with the grid spacing increasing from 20 m at the surface to 380 m above 10-km height. The ground surface is flat, and the model top is at 16 km AGL. The first scalar variable level is 10 m AGL. Fourth-order centered scheme is applied to the advection of momentum, while scalar variables including the potential temperature, water variables, and subgrid-scale turbulent kinetic energy (TKE) are advected by a fully multidimensional flux-corrected transport (FCT) scheme that is a nonlinear combination of fourth-order and first-order schemes. The FCT scheme is monotonic and is, therefore, also positive definite for positive quantities such as water vapor. Microphysics is parameterized using the five-species ice scheme of Lin et al. (1983), with default intercept parameter of cloud water, rainwater, ice, snow, and hail. Subgrid-scale turbulence is parameterized using the 1.5-order TKE formulation of Moeng and Wyngaard (1988), and fourth-order computational mixing is employed. All simulations are integrated for 2 h. The above configurations are similar to those of Roberts et al. (2016, hereafter R16) but with different domain size, horizontal grid spacing, rain intercept parameter value, and the scalar advection scheme used.

Surface drag or friction is included in the simulations with a constant drag coefficient (C_d) of 0.02. This value is typical of relatively rough land surface. As described in R16, surface drag is included in the ARPS model as horizontal momentum stresses for the x and y directions defined at the ground surface, and the direct effect of the drag comes into the model as the momentum flux divergence in the vertical subgrid-scale turbulence parameterization terms for momentum. While almost all idealized storm simulations referenced in introduction ignored the

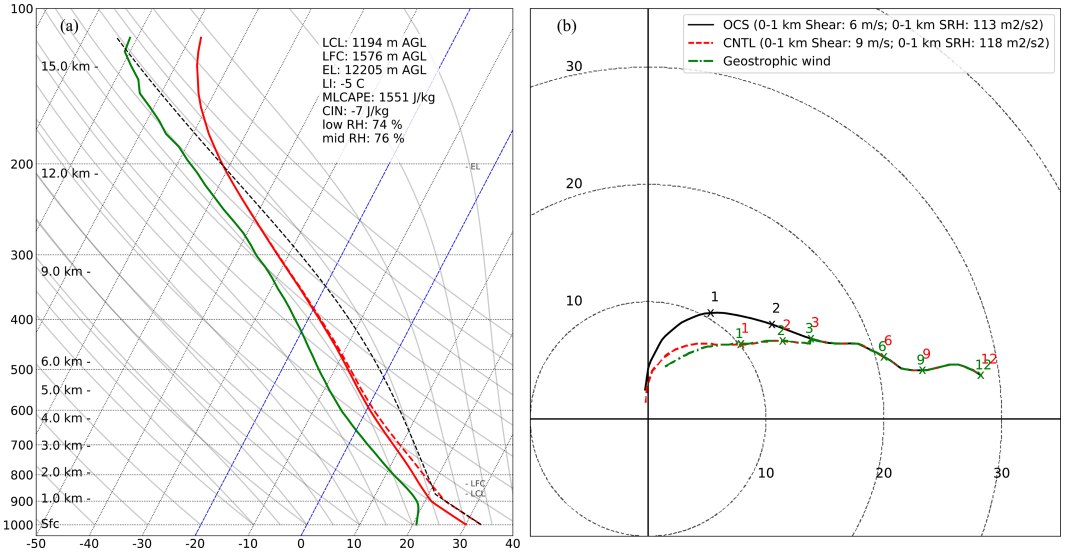

FIG. 1. (a) Skew T diagram for CNTL based on the composite sounding of SIGTOR of China. The temperature, dewpoint, virtual temperature, and parcel trace are denoted by solid red, solid green, dashed red, and dashed black lines. Dashed blue lines denote 0° and −20°C isotherms. The "low RH" and "mid-RH" refer to the mean RH from the surface to 850 hPa and from 850 to 700 hPa, respectively. (b) Composite hodographs for the OCS (solid black), the geostrophic wind (dotted–dashed green), and the balanced wind profile used in CNTL (dashed red) up to 12 km AGL. Labels on the curves denote the heights AGL in kilometers. The wind speed unit is meters per second. The 0–1-km vertical wind shear and SRH are given in the legend, except geostrophic wind.

surface drag, recent studies have shown that surface drag can have a significant effect on tornado dynamics, including acting as an important source of near-surface vorticity generation for tornadogenesis (e.g., Schenkman et al. 2014; R16; Roberts and Xue 2017; Roberts et al. 2020; Tao and Tamura 2020; Jiang and Dawson 2023). More and more researchers have started to include it in their idealized storm simulations (e.g., Markowski 2016; Dawson et al. 2019; Fischer and Dahl 2022; Coffer et al. 2023), while real-data tornado simulations naturally include surface friction as part of surface-layer parameterization (e.g., Schenkman et al. 2014; Yokota et al. 2018; Tao and Tamura 2020). Additionally, the Coriolis force is included. The background horizontal pressure gradient force is specified in terms of the background geostrophic wind.

The horizontally homogeneous environment of all experiments is based on a regional composite sounding for SIGTOR within China from 1980 to 2016 (Zhang et al. 2023) with some modifications, which will be described in next subsection. For every experiment, a constant wind speed is subtracted from the input sounding to keep the simulated storm near the center of model domain. This subtracted wind speed is obtained as the average storm motion speed between 1400 and 2900 s of a trial simulation using the original sounding, and it is often called grid translation speed, while the model wind is grid relative. In the calculation of surface drag, ground-relative wind speed is always used.

Convection in the model is triggered by an ellipsoidal thermal perturbation centered at $x = 40$ km, $y = 40$ km, and $z = 1.5$ km. The ellipsoid has a radius of 10 km in the horizontal and 1.5 km in the vertical, and the maximum potential temperature perturbation is 6 K at the center. This relatively large temperature perturbation is used to ensure that the triggered cell can at least develop into deep convection through its initial phase even when the environment is less favorable. The same temperature perturbation and bubble size and height were used in R16 and related studies.

b. *Modified sounding for control experiment*

The initial environmental sounding used in this study comes from the composite of 93 significant tornado cases within China for the period of 1980–2016 with TC tornado cases removed. The tornado proximity soundings are extracted from the fifth generation ECMWF atmospheric reanalysis (ERA5) pressure-level dataset with 1-h time resolution, and readers are referred to Zhang et al. (2023) for more details on the sounding extraction. After subjectively checking the hodograph of each tornado sample, we eliminate additional 32 cases where the hodographs appear unrealistic. For example, the wind shear between 1 and 12 km is less than 5 m s^{-1} in some cases. This step makes the composite sounding more representative. Ultimately, this original composite sounding (OCS) of total 61 SIGTOR samples serves as the basis for further modifications for subsequent sensitivity experiments.

We decrease the CIN of OCS to zero by keeping the potential temperature constant (a neutral stratification) below 1 km to facilitate convective initiation and maintenance in the absence of any mesoscale forcing, as many idealized simulations do (e.g., Gilmore and Wicker 1998; Xue et al. 2001; R16). The resulting thermodynamic sounding profiles are shown in Fig. 1a.

With the inclusion of surface drag, the environmental wind profile near the surface in typical idealized simulations will be gradually modified unless the wind profile is already in a

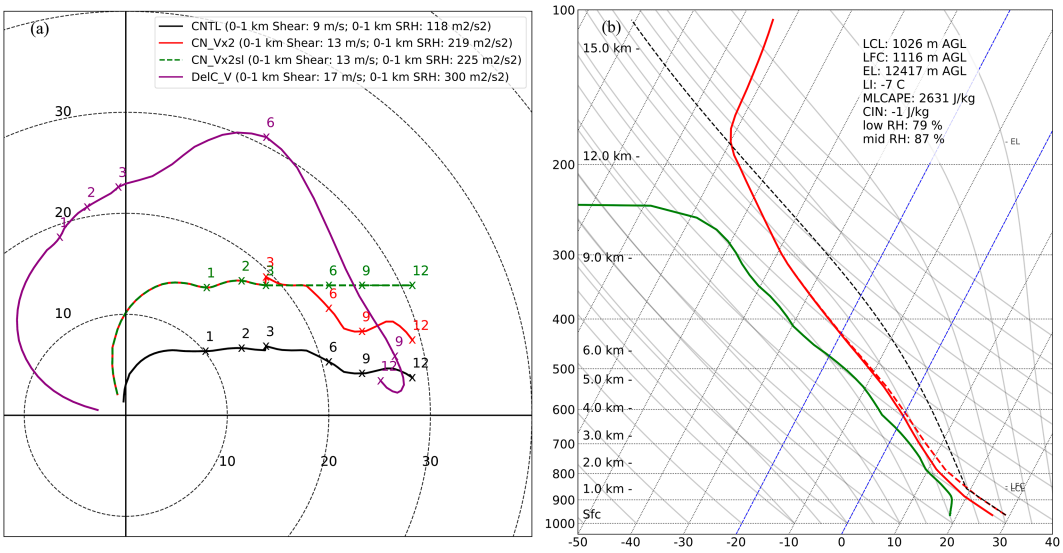

FIG. 2. (a) Hodographs used by experiments CNTL (the original spinup profile, solid black), CN_Vx2 (v component doubled, solid red), CN_Vx2sl (straightened upper level, dashed green), and DelC_V (Del City wind profile, solid purple). (b) The skew T plot of the Del City thermodynamic sounding (see also caption as in Fig. 1a).

three-way geotriptic balance among frictional, Coriolis, and pressure gradient forces (Johnson 1966). This "complicates interpretation of the results" (Dawson et al. 2019) when studying the sensitivity to the environmental conditions defined by the sounding. Here, we run a "spinup" procedure similar to that used in R16 to obtain a wind profile that is in a geotriptic balance at levels where frictional resulting from surface drag is present; such an environmental wind profile will remain nearly unchanged during the simulations. Further details on the balance procedure are given in the appendix. The final balanced wind profile is shown as a red dashed line in Fig. 1b, while the original profile is in solid black. The average geostrophic wind profile calculated from the pressure fields of ERA5 data and used in the spinup procedure is shown as the green dotted–dashed line in Fig. 1b. The temperature and moisture profiles used in control (CNTL) experiment are plotted in Fig. 1a.

c. *Sensitivity experiments*

As mentioned in introduction, a series of initial sensitivity experiments were run first. In experiment CN_Vx2, the north–south wind component v is doubled from that of the original geostrophic wind (cf. Fig. 1), and after the spinup procedure, the hodograph labeled CN_Vx2 in Fig. 2a is produced, which primarily enhances low-level wind shear and SRH. In CN_Vx2sl, the upper portion of the CN_Vx2 hodograph is straightened to resemble the commonly used quarter-circle hodograph (e.g., Klemp and Weisman 1983; Droegemeier et al. 1993; Fig. 2a). Moreover, in experiment DelC_V, the wind profile from the well-known 20 May 1977 Del City, Oklahoma, tornadic storm (Ray et al. 1981) is used to replace that of the OCS. The Del City sounding is known to produce sustained supercell storms in many prior studies (e.g., Klemp et al. 1981), including that with the same model used in this study (Xue et al. 2001). Note that, unlike the previous wind profiles processing, the initial Del City wind profile is assumed to be geostrophic, following the approach of R16. Additionally, in experiment DelC_TQ, the temperature and moisture profiles of CNTL are replaced with those from the Del City sounding (Fig. 2b), while the wind profile from CNTL is retained.

The next set of experiments focuses on modifying humidity in various layers relative to CNTL. Specifically, we examine the 1–3-km layer AGL, since sensitivity to RH in this layer remains poorly understood and its moisture has minimal influence on parameters such as LCL and CAPE. In experiment CN_M13, the RH in the 1–3-km layer AGL is set to the commonly used analytical profile of Weisman and Klemp (1982), ranging from 85% to 97% (Fig. 3a). As expected, this adjustment leaves LCL and mixed-layer CAPE (MLCAPE) largely unchanged from CNTL (cf. Fig. 1a). In experiments CN_M23 and CN_M12, the RH within the 2–3-km and 1–2-km layer AGL, respectively, is modified instead (Figs. 3b,c). In CN_D12, RH in the 1–2-km layer AGL is decreased by the same amount that is increased in CN_M12, relative to CNTL (Fig. 3d). In these RH modification experiments, adjustment to low-level RH substantially alters the specific humidity q_v within the initial thermal bubble due to its higher temperature, resulting in different initial storm responses. In particular, storms exhibit a noticeably stronger initial intensity when moisture is enhanced. Another set of corresponding experiments, CN_M13nb, CN_M12nb, CN_M23nb, and CN_D12nb, are also performed in which RH modification is not applied within the initial bubble. Table 1 lists key parameters of the soundings. Small differences are found in MLCAPE and LCL of experiments like CN_Vx2 from CNTL because of differences in the mixing effect during sounding spinup.

d. *Calculation of water vapor entrainment*

As mentioned in introduction, we calculate the entrainment rate of water vapor mass (ρq_v, where ρ is the air density) into

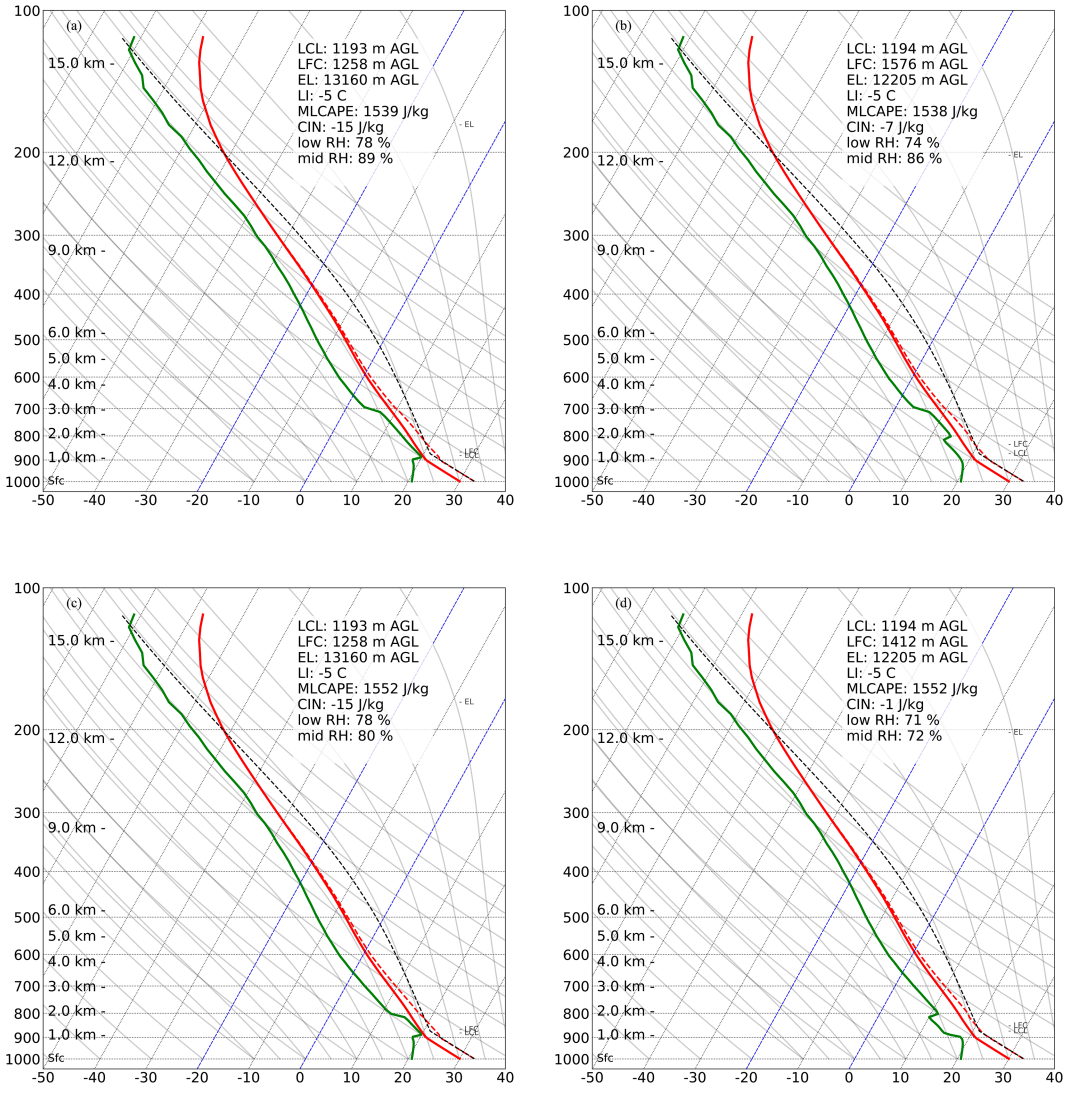

FIG. 3. As in Fig. 1a, but for soundings used in (a) CN_M13, (b) CN_M23, (c) CN_M12, and (d) CN_D12.

the updraft core, rather than the entrainment rate of air mass (ρ), as our focus is on the amount of moisture entering or exiting the updraft core. Because of the nonconservation of ρq_v, the method of Dawe and Austin (2011a) that relies on mass conservation is not applicable here. Instead, we developed a new, more straightforward method for calculating the water vapor flux through the updraft core surface. Rather than computing the moisture flux through an arbitrarily oriented

TABLE 1. Parameters of the soundings used in different experiments.

Experiments	0–1-km shear ($m\ s^{-1}$)	0–1-km SRH ($m^{-2}\ s^{-2}$)	0–6-km shear ($m\ s^{-1}$)	0–3-km SRH ($m^{-2}\ s^{-2}$)	1–2-km avg RH (%)	2–3-km avg RH (%)	MLCAPE ($J\ kg^{-1}$)	LCL (m)	CIN ($J\ kg^{-1}$)
CNTL	9	118	20	166	82	74	1551	1194	−1
CN_Vx2	13	219	22	270	82	74	1535	1201	−8
CN_Vx2sl	13	225	23	270	82	74	1535	1201	−8
DelC_V	17	300	31	379	82	74	1508	1210	−9
DelC_TQ	9	118	20	166	87	88	2631	1026	−1
CN_M13/CN_M13nb	9	120	20	168	94	88	1539	1193	−15
CN_M12/CN_M12nb	9	120	20	168	93	74	1552	1193	−15
CN_M23/CN_M23nb	9	118	20	166	83	88	1538	1194	−7
CN_D12/CN_D12nb	9	118	20	166	83	88	1538	1194	−1

surface within a grid cell, we approximate the total flux as the sum of the fluxes through the x-, y-, and z-oriented faces of each grid cell. To improve the accuracy of such approximation, each grid cell is subdivided into finer subcells, e.g., into $3 \times 3 \times 3$ or $9 \times 9 \times 9$ or more subcells. The values of q_v and velocity components are linearly interpolated to these subcells while preserving the C-grid staggering. An illustration of this approach for a 2D grid cell in the x–z plane is provided in Fig. 4. The updraft core is defined as the consecutive locations where vertical velocity exceeds 2 m s^{-1} (following the threshold of LT21), while a hydrometeor threshold is not imposed (following JLT23). In this work, each grid cell is uniformly subdivided into 729 subcells (nine in each of three directions). A subcell is classified as part of the updraft core if w at its center exceeds the predefined threshold. The interfaces between core and noncore subcells then approximate the boundary of updraft core. As illustrated in Fig. 4, when grid cells become finer, the calculation of flux across the core boundaries becomes increasingly more accurate. In practice, the water vapor flux through the east–west face of a boundary cell (indicated by the red lines in Fig. 4) is given by

$$F_{q_v} = \int \rho q_v u dA, \tag{1}$$

where u is the x component of velocity and A is the area of the cell face. For the eastern (western) boundary of the updraft core, F_{q_v} less (greater) than 0 signifies inflow or entrainment, whereas F_{q_v} greater (less) than 0 signifies outflow or detrainment. The same principle applies to the other faces of boundary cells. Our time interval of model output is 10 s, with six-sample averaging yielding 1-min average water vapor entrainment rates.

In this study, moisture flux through the updraft core surface below the LCL is also considered part of water vapor entrainment. Many other studies (e.g., Romps 2010; Moser and Lasher-Trapp 2017; LT21; Jo and Lasher-Trapp 2022; JLT23) define entrainment strictly as fluxes above the LCL, treating those below as part of the primary updraft. Generally, there is more air entering the cloud body or updraft core from below the LCL, and this air tends to have higher equivalent potential temperature (more potential energy). This is why the entrainment values of lower levels are often much larger (e.g., LT21, their Fig. 10). However, to comprehensively assess the effect of moisture flux on storm evolution, contributions from both above and below the LCL must be considered. Furthermore, some of the moisture entering the cloud from below the LCL may originate from above the LCL via recirculating air, making it difficult to distinguish between lateral and vertical fluxes. Since all water vapor entrained into the updraft core—regardless of direction—contributes to condensate formation and latent heat release (JLT23), it plays a crucial role in enhancing convection. Therefore, the difference in the definition of entrainment adopted in this study relative to most previous work should be clearly noted.

3. Simulation results

a. *Results of control simulation*

A concise overview of the control simulation is provided in this subsection. With the moderate wind shear and CAPE in

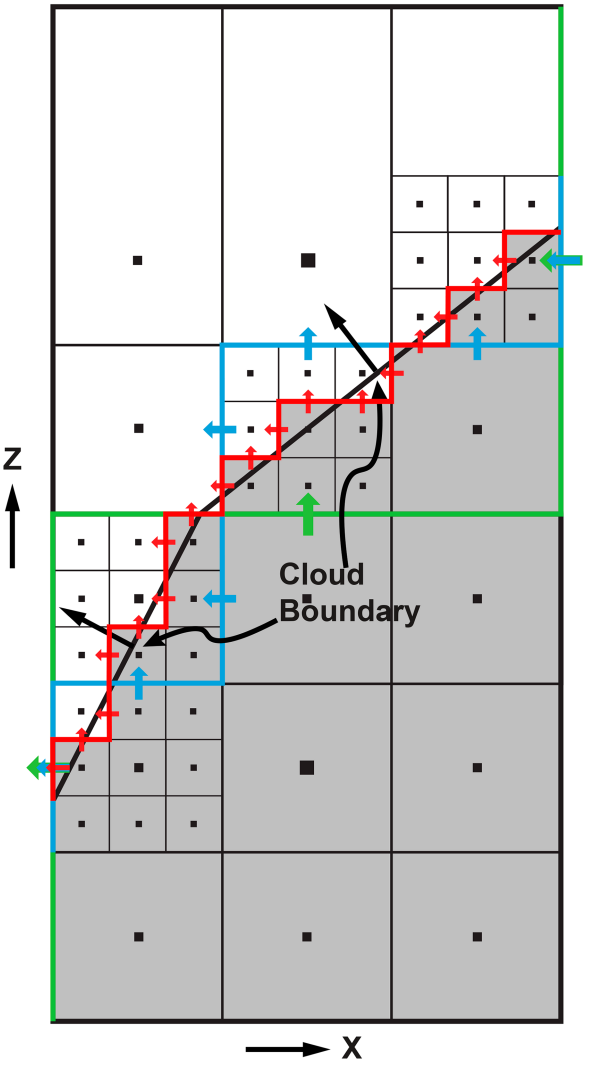

FIG. 4. Two-dimensional illustration of the calculation of water vapor flux through a cloud or updraft boundary shown as two segments of straight black lines within two grid cells stacked on top of each other. The fluxes through the two segments (in their normal outward directions indicated by the twov large arrows) can be approximated as the sum of fluxes through the boundaries of the grid cells that the boundary passes through. When the center of a grid cell falls within the cloud or updraft (below the boundary in the above example, shaded), that cell is considered inside the boundary completely and the fluxes on the left and upper boundaries are calculated. When the cell center is outside the boundary, that cell is considered entirely outside, and the fluxes through the lower and right boundaries are calculated. When calculating on the original two grid cells, the approximate total flux is calculated as the sum of the fluxes indicated by the three green arrows. The approximation can be improved by successively refining the grid, subdividing each grid cell into 3×3 cells. Doing this once, the two grid cells are divided into 18 cells. The total flux is equal to the sum of fluxes indicated by the seven blue arrows through the cell boundaries. Performing another level of cell refinement, the total flux is equal to the sum of fluxes indicated by 19 red arrows. The procedure can be programmed with relative ease, and the grid can be refined to any level to achieve desired accuracy, but in general, two levels of refinement are enough.

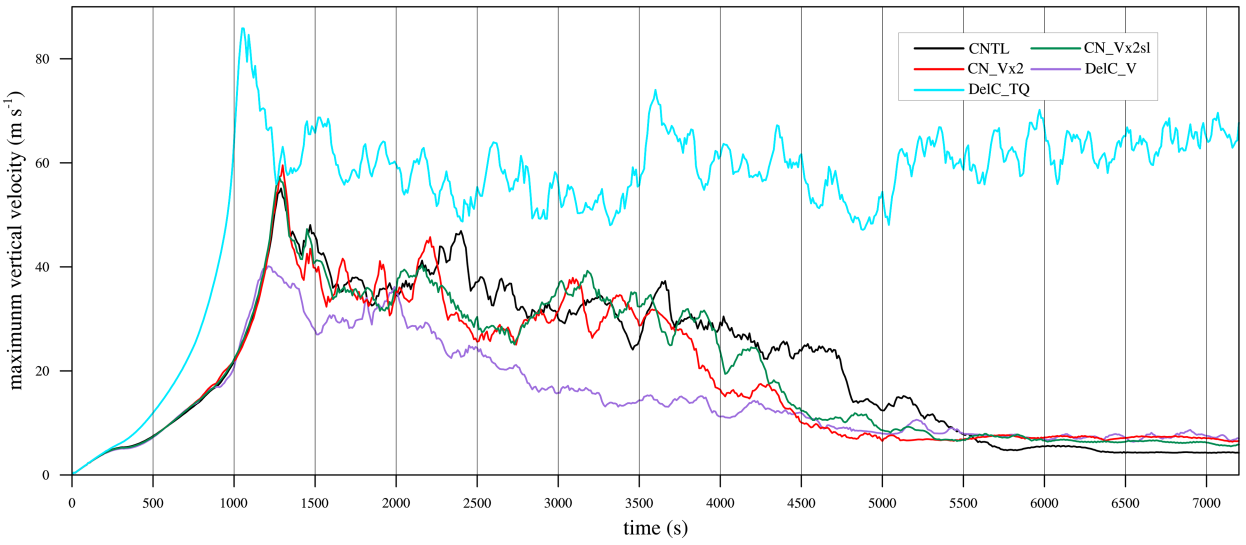

FIG. 5. Time series of maximum vertical velocity for CNTL (solid black), CN_Vx2 (solid red), CN_Vx2sl (solid green), DelC_V (solid purple), and DelC_TQ (solid blue).

CNTL sounding (Fig. 1), a relatively short-lived (~1.5 h) convective system gradually decays, after the updraft driven by the initial thermal bubble reaches its initial peak at ~1300 s (Fig. 5). At later stages of the simulation, few convective cells form along the low-level outflow boundary. The initially single cell (Fig. 6a) begins to split around 3000 s (Fig. 6b), and by 3900 s (Fig. 6c), two distinct storm cells have formed. The northern storm cell (left mover) stays close to the outflow boundary, while the southern cell (right mover) is more than 10 km behind the gust front located to its southeast (Fig. 6c) at this time. By 4800 s, the two split cells drift further apart and become weaker, especially the southern cell (Fig. 6d), with the maximum updraft velocity w_{max} falling below 15 m s^{-1} (Fig. 5). By 5400 s, both storm cells have dissipated (Fig. 6e). Figure 5 shows that w_{max} drops substantially at around 4750 s and stays below 7 m s^{-1} after 5750 s, indicating a complete decay of the storms. There is a general decreasing trend of CNTL w_{max} after 2500 s.

It is worth noting that, despite the cyclonically curved hodograph in CNTL (cf. Fig. 1b), the left-moving storm remains stronger and persists somewhat longer than the right mover throughout the simulation (Figs. 6c–e). Similar behavior has been reported in some earlier studies (Weisman and Klemp 1984; Grasso and Hilgendorf 2001; Bunkers 2002), although detailed discussions of this phenomenon have been limited. Based on the classic theory advanced by Rotunno and Klemp (1982), in an environment of nonunidirectional vertical shear with clockwise-curved hodograph, linear perturbation vertical pressure gradient force (VPGF) due to the interaction between the storm updraft and the environmental wind shear would promote the right mover more than the left mover, leading to a stronger right-moving cell. The fact that the left mover is stronger in CNTL simulation suggests that something else plays a bigger role than the dynamic pressure perturbation predicted by the linear theory. The cold pool–inflow interactions and their effect on the lifted updraft may have played a more dominant role (see section 3e). The distance between the storm cell and gust front, which lifts the inflow air feeding the respective updraft, appears to be a critical factor. This aspect is discussed further in section 3e, while the exact mechanisms underlying the behaviors warrant further investigation in future studies. In the present work, we focus on the evolution of the overall storm system, with the goal of identifying which aspects of the environmental sounding most strongly influence the longevity of the simulated storms.

b. *Sensitivity of simulated storms to hodographs*

It is well established that stronger low-level shear promotes the development of more intense and long-lived supercell storms (e.g., Rotunno and Klemp 1982; Davies-Jones 1984; Weisman and Rotunno 2000). Cyclonically curved hodographs would further promote the right-moving cell through dynamic pressure effects (Klemp 1987) and increase in low-level SRH (Rotunno 1981; Davies-Jones 1984). The relative weaker low-level shear in the CNTL hodograph was initially suspected to contribute to the failure of sustaining simulated storms. The doubling of v velocity of the CNTL hodograph in CN_Vx2 yields much larger low-level shear and SRH and a more cyclonically curved hodograph (Fig. 2a and Table 1). The 0–1-km SRH reaches 219 m^2 s^{-2}, falling within the range supportive of significant tornadoes (Thompson et al. 2012). However, contrary to expectations, the storm longevity does not improve in CN_Vx2. Instead, w_{max} starts to decline rapidly around 1 h into the simulation (Fig. 5). The evolution of this storm generally resembles that of CNTL, splitting into two cells around 3000 s. The left mover is also stronger, and both storm cells are fully dissipated by 5400 s (left column in Fig. 7). Additional differences exist in the storm morphologies between CNTL (Fig. 6) and CN_Vx2 (Fig. 7).

The hodograph of CN_Vx2sl closely resembles the commonly used quarter-circle hodograph, which has been shown to support sustained storms with a preferential enhancement of

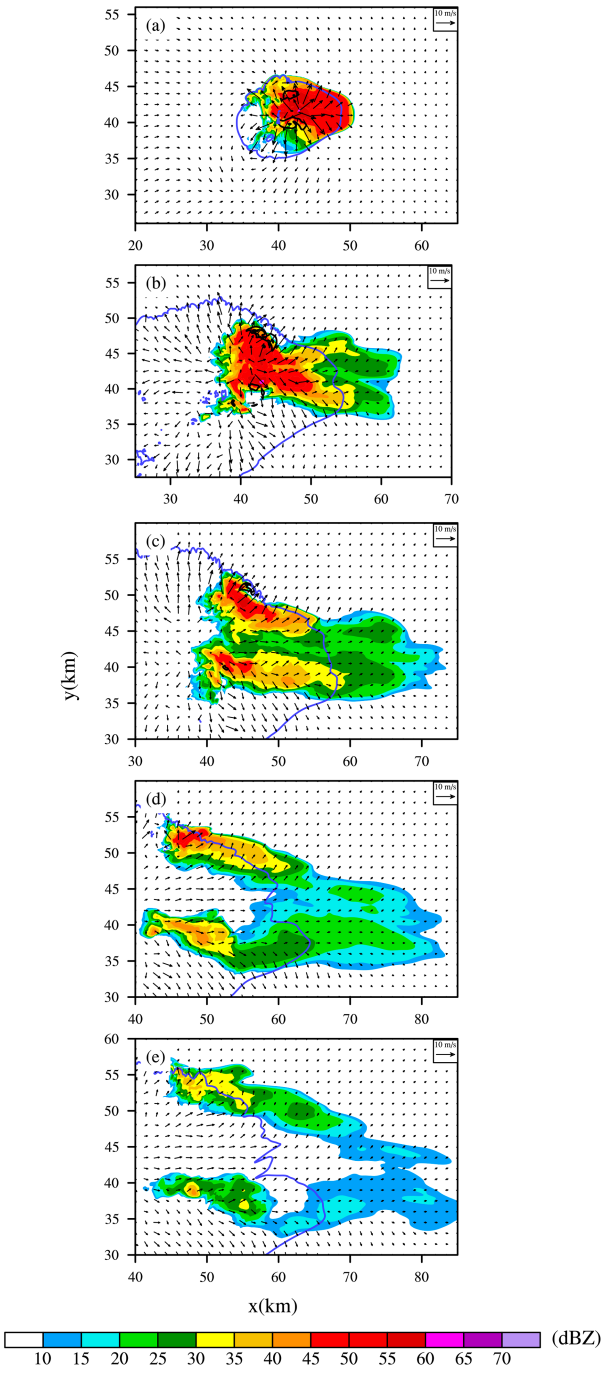

FIG. 6. Simulated radar reflectivity (shaded) and perturbation (from environmental sounding) wind vectors at the first model level above the ground (10 m AGL) for CNTL at (a) 1800, (b) 3000, (c) 3900, (d) 4800, and (e) 5400 s. The solid blue contours are for the −1-K potential temperature perturbation and indicate the outflow boundaries. The solid black contours depict the 10 and 15 m s^{-1} vertical velocity at 3 km AGL.

the right mover (Rotunno and Klemp 1982; Weisman and Klemp 1986; Droegemeier et al. 1993). Nevertheless, even with this hodograph, the right mover remains weaker and less persistent than the left mover, and the overall convective system is still short-lived (middle column, Fig. 7). Compared to CN_Vx2, the cloud anvil in CN_Vx2sl is oriented mostly eastward instead of east-southeastward, due to the wind direction change at the upper levels. This change also appears to affect the separation of the split cells, with the right mover in CN_Vx2sl deviating more slowly to the right than in CN_Vx2. (Figs. 7j,k).

The Del City hodograph used in DelC_V features strong directional shear overall, including enhanced 0–1-km shear and SRH values of 17 m s^{-1} and 300 m^{-2} s^{-2}, respectively (Table 1). Despite these favorable shear conditions, the simulated storms with DelC_V are even weaker and short-lived. The initial w_{max} peak reaches only ~40 m s^{-1} (Fig. 5), and the storm system largely dissipated by 3900 s (Fig. 7i). The right-moving storm is notably stronger and long-lasting than the left mover. Different from simulations using the original Del City thermodynamic sounding (Xue et al. 2001), the stronger right mover is positioned far behind instead of being close to the southeastern edge of the cold pool (Fig. 7f), which appears to be the reason for its quick dissipation.

c. *Sensitivity of simulated storms to moisture profiles*

The results from the previous subsection suggest that the failure to simulate sustained storms is more likely associated with the environmental temperature and moisture profiles. To examine this hypothesis, we conducted an experiment that is identical to CNTL, except that it adopts the temperature and moisture profiles from the original Del City sounding (cf. Fig. 2b), named DelC_TQ. In this experiment, the simulated storms maintain strong intensity, with w_{max} maintained at ~60 m s^{-1} (Fig. 5), and the right mover exhibits clear supercell characteristics throughout the 2-h simulation (Fig. 8). A notable feature of the Del City sounding is the relatively moist layer between 850 and 750 hPa (Fig. 2b). Similarly, the widely used analytical sounding of Weisman and Klemp (1982) also features very high RH (ranging from 96.6% to 86.7%) in the 1–3-km layer AGL (see Fig. 3a). Numerous sensitivity studies based on the Weisman and Klemp (1982) sounding (e.g., McCaul and Weisman 2001; McCaul and Cohen 2002) further simplified the moisture profile by setting RH above the LCL to 90%. Additionally, Chavas and Dawson (2021) showed that enhancing humidity within the free troposphere can turn short-lived storms into long-lived ones.

These prior findings, together with our earlier results, motivated a focused investigation into environmental humidity—especially low-level humidity—as a potentially critical factor influencing storm intensity and longevity.

Compared to CNTL, the increase of 1–3-km RH in CN_M13 led to a substantial improvement in storm maintenance. Following the initial cell development, w_{max} remains between 40 and 55 m s^{-1} throughout the 2-h simulation (Fig. 9), consistent with the effects observed in Chavas and Dawson (2021). Specifically, in CN_M13, the first peak of w_{max} reaches approximately

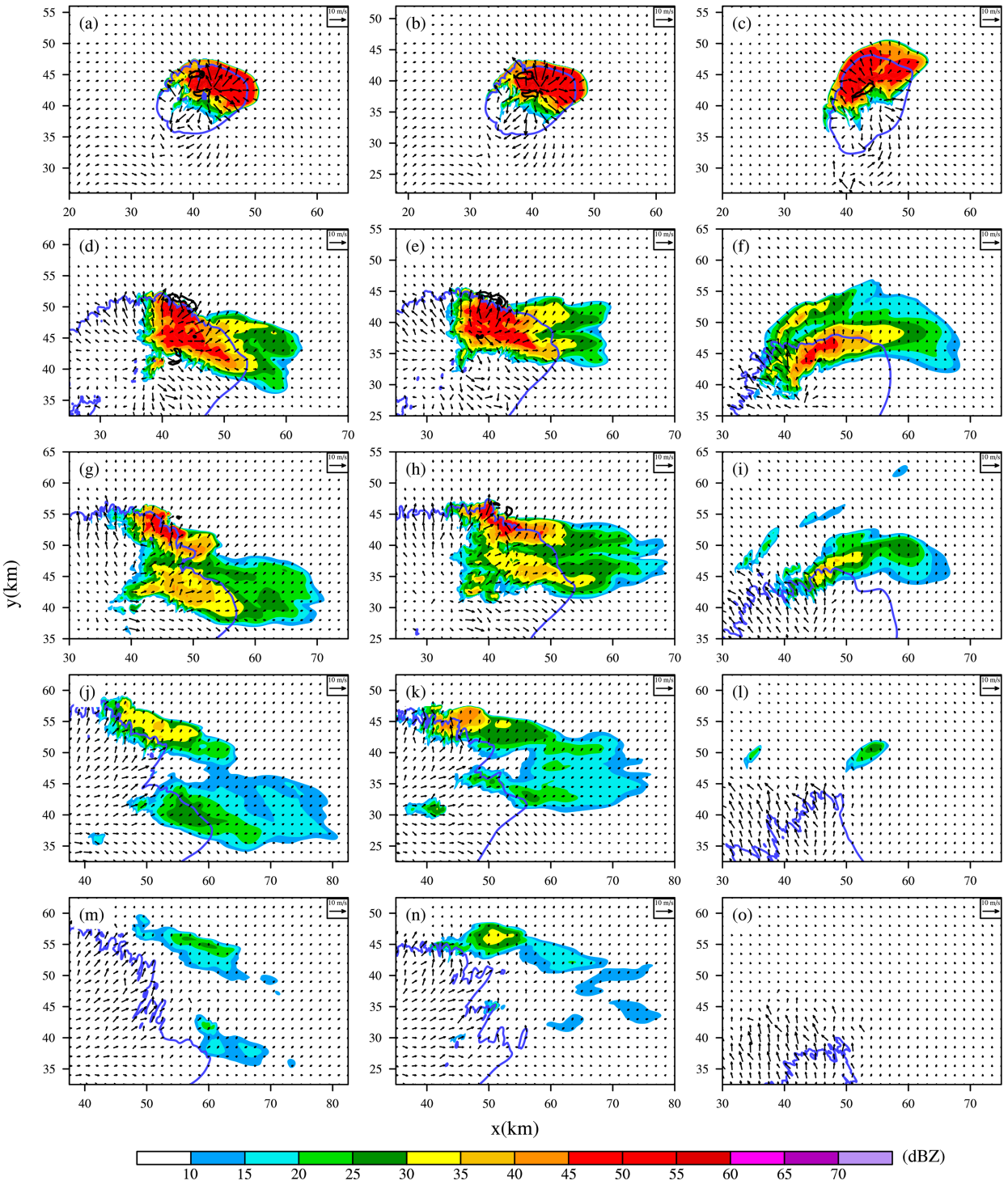

FIG. 7. As in Fig. 6, but for (left) CN_Vx2, (middle) CN_Vx2sl, and (right) DelC_V at (top)–(bottom) 1800, 3000, 3900, 4800, and 5400 s.

65 m s^{-1}—significantly higher than the ~54 m s^{-1} observed in CNTL—and occurs about 200 s earlier. Large morphological differences exist between the storms in CN_M13 and CNTL. The right-moving storm no longer dissipates prematurely and is, in fact, stronger than the left mover (Fig. 10j), as expected for a cyclonically curved hodograph (e.g., Klemp and Wilhelmson 1978; Rotunno and Klemp 1982). The right mover remains close to the gust front throughout the simulation, particularly after 3000 s. It develops a classic hook echo, with strong reflectivity extending southward behind the

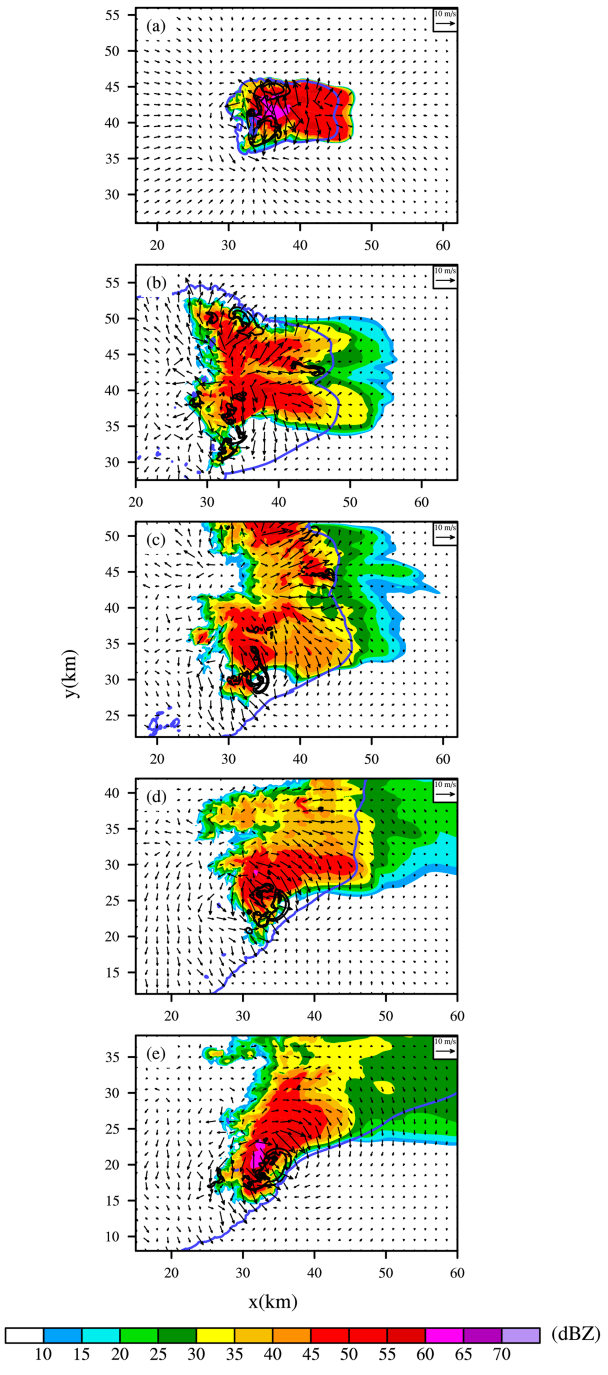

FIG. 8. As in Fig. 6, but for DelC_TQ at 1800, 3000, 3900, 5400, and 6400 s.

rear-flank gust front (RFGF) and weaker reflectivity spreading eastward into the anvil region behind the forward-flank gust front (FFGF). This close proximity to the gust front likely plays a key role in sustaining the storm intensity, as inflow lifted by the gust front is directly fed into the upright updraft. Another important difference is that the right and left movers in CN_M13 move southward and northward much more than in CNTL (Fig. 10g vs Fig. 6e); the larger sideward storm motion, relative to the deep-layer wind shear, contributes to higher SRH in the inflows feeding the storm cells (Rotunno 1981; Klemp 1987). Overall, the right-moving storm exhibits structural features characteristic of classic supercells, including the hook echo (Fig. 10g, Lemon and Doswell 1979).

Figure 9 shows that in CN_M23, where moisture is enhanced in the 2–3-km layer AGL, w_{max} closely follows that of CNTL, and the simulated storms remain short-lived. In contrast, w_{max} in CN_M12 closely resembles that in CN_M13, with storms maintaining strong intensity throughout the 2-h simulation. In terms of the low-level fields, including the reflectivity, the results from CN_M12 (middle column in Fig. 10) are very similar to those of CN_M13 (left column in Fig. 10), with the primary difference being a somewhat weaker left mover in CN_M12. These results indicate that moisture in the 1–2-km layer AGL is critical; notably, this layer lies just above the mixed layer, whose top is slightly below the LCL (1193 m). When moisture is enhanced in the 2–3-km layer AGL, it has little effect on the longevity of simulated storms. Clearly, the intensity and longevity of the simulated storms are most sensitive to moisture in the 1–2-km layer AGL. As expected, the simulated storms in CN_D12 are even weaker than those in CNTL, with peak w less than 40 m s^{-1} and the updraft becoming very weak after 2500 s (Fig. 9). The corresponding simulated fields are not shown. In the next subsection, we analyze in more details of how the moisture in the layer above 1 km affects the storm intensity and evolution.

d. *The effect of moisture in initial warm bubble*

Figure 9 shows that w_{max} increases noticeably faster in CN_M12 and CN_M13 than in the other experiments after ~300 s, coinciding with the onset of significant condensational heating. The initial peak w associated with the initial thermal bubble is about 10 m s^{-1} higher. This is because the RH enhancement applied to the initial condition increases q_v within the bubble even more, as previously discussed. As a result, the maximum buoyancy in the initial storm updraft is substantially enhanced. To avoid this effect, we set q_v within the bubble, where initial θ' exceeds 3.2 K to the original value of CNTL in corresponding experiments named CN_M12nb, CN_M23nb, CN_M13nb, and CN_D12nb (Table 1).

Figure 11 shows that the buoyancy in terms of θ' in the updraft core of CN_M12nb closely matches that of CNTL during the early stage while that of CN_M12 is much higher. Figure 12 shows that the first peak of w_{max} and its timing are nearly identical among the CN_M13nb, CN_M12nb, CN_M23nb, CN_D12nb, and CNTL simulations. The first peak of w_{max} of CN_D12nb is substantially enhanced compared to CN_D12 (cf. Fig. 9). Therefore, particular attention should be given to the humidity within the initial bubble when modifying the environmental condition, which may influence subsequent evolution of simulated storms (Flournoy and Rasmussen 2023). In our case, the overall evolutions of the storm systems in the corresponding pairs (CN_M13 vs CN_M13nb and CN_M12 vs CN_M12nb) are almost unchanged after the initial peak except for a slight decrease in the intensity of CN_M12nb at the end

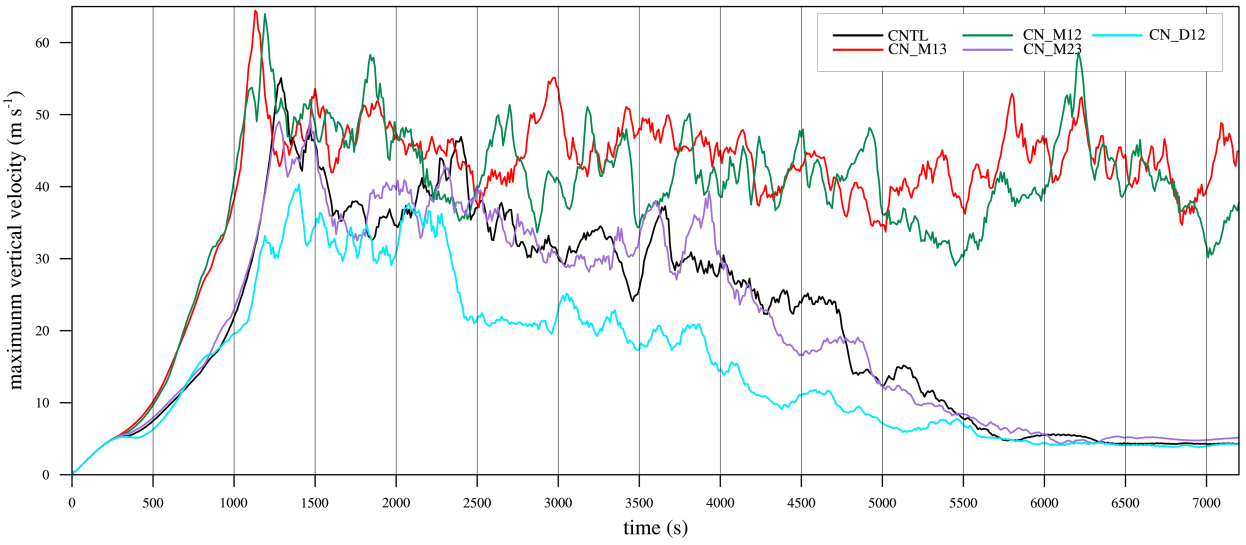

FIG. 9. Time series of maximum vertical velocity for CNTL (solid black), CN_M13 (solid red), CN_M12 (solid green), CN_M23 (solid purple), and CN_D12 (solid blue).

of the 2-h simulation (Fig. 12 vs Fig. 9 and Fig. 13k vs Fig. 10k). In the rest of this paper, we will focus on analyzing the results of experiments CN_M13nb, CN_M12nb, CN_M23nb, and CN_D12nb.

e. *The effect of mid–lower-level environmental water vapor*

Similar to CN_M13 and CN_M12, the right movers in CN_M13nb and CN_M12nb remain close to the RFGF later on (Fig. 13), a key distinction from CNTL (Fig. 6) as previously noted. Several factors may contribute to the right mover being positioned far behind the RFGF in CNTL: 1) excessively strong evaporative cooling associated with the dry layer, which generates outflow that aggressively overruns the updraft; 2) a much weaker updraft does not draw in as much low-level inflow or cause associated inflow acceleration, thereby reducing the ability for the inflow to counteract the forward propagation of the gust front; and 3) a combination of these factors and potentially other factors. To further explore the effects of increasing above-LCL humidity on simulated storms, we select several times during the storm development stage (~1200–2200 s) of CN_M12nb and CNTL for the comparative analysis.

The effect of evaporation cooling on outflow should be directly reflected in the strength of the surface-based cold pool. We calculate parameter C as a measure of the cold pool strength for CN_M12nb and CNTL where $C^2 = 2\int_0^H(-B)dz$, with B being the buoyancy within the cold pool of depth H (Weisman 1992). The buoyancy includes water loading, virtual temperature, and pressure perturbation effects as calculated in the ARPS model. The C is also associated with the theoretical propagation speed of density current (cold pool) relative to inflow.

At 1500 s, the cold pools—approximately delineated by the −1-K θ' contour—exhibit similar maximum strengths in both simulations, although the cold pool in CNTL has a somewhat larger extent. The 3125-m updraft core of the right mover in CN_M12nb is positioned farther southeast relative to the cold pool (Fig. 14a), whereas in CNTL, it is located farther back to the west (Fig. 14b). By 1800 s, the cold pools have expanded in both cases with CN_M12nb showing stronger maximum intensity in terms of C (Figs. 14c,d) due to more precipitation, and both simulations reach a similar minimum θ' of approximately −8.4 K (not shown). By 2200 s, the difference in cold pool strength becomes more pronounced (Figs. 14e,f), with the minimum θ' in CN_M12nb (−8.4 K) being slightly lower than that in CNTL (−8.2 K). Therefore, the relative dryness in CNTL does not enhance the cold pool via evaporative cooling but on the contrary produces a weaker cold pool because of less precipitation (Fig. 6a vs Fig. 13b). Similar behavior was seen in James and Markowski (2010), where cold pool was weaker in drier environments with lower CAPE.

Although a stronger cold pool generally propagates forward more rapidly, the RFGFs of the right movers in CN_M12nb and CNTL occupy very similar positions at 1800 and 2200 s (Fig. 14). The stronger perturbation inflow winds in CN_M12nb (Figs. 14c–f), indicative of enhanced storm intensity, may counteract the expected faster propagation of the stronger cold pool, resulting in a similar gust front position to that in CNTL. This allows the updraft in CN_M12nb to remain much closer to the gust front.

Figure 15 shows the vertical cross sections along the black straight lines in Fig. 14, roughly through the midlevel updraft core of the right mover in CN_M12nb and CNTL. At 1500 s, the updraft in CN_M12nb is more upright in the lower layers and extends deeper overall compared to CNTL. Additionally, a portion of the updraft in CN_M12nb is located ahead of the surface gust front, whereas in CNTL, the updraft remains almost entirely behind it (Figs. 15a,b). For example, at 3-km altitude, the maximum w in CN_M12nb is located near $x = 9.5$ km, roughly above the leading edge of the cold pool. In contrast, in

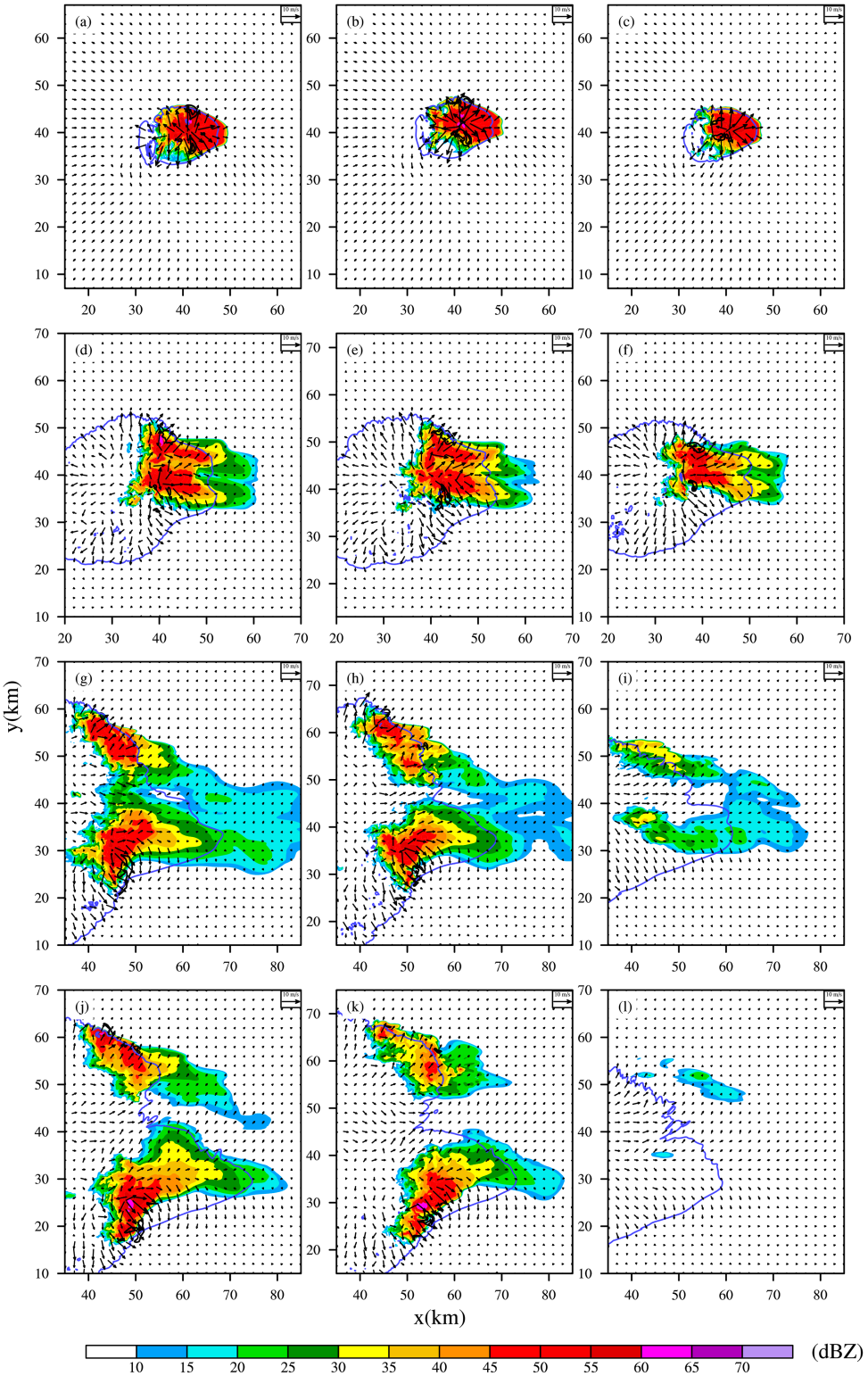

FIG. 10. As in Fig. 6, but for (left) CN_M13, (middle) CN_M12, and (right) CN_M23 at (top)–(bottom) 1800, 3000, 5400, and 6400 s.

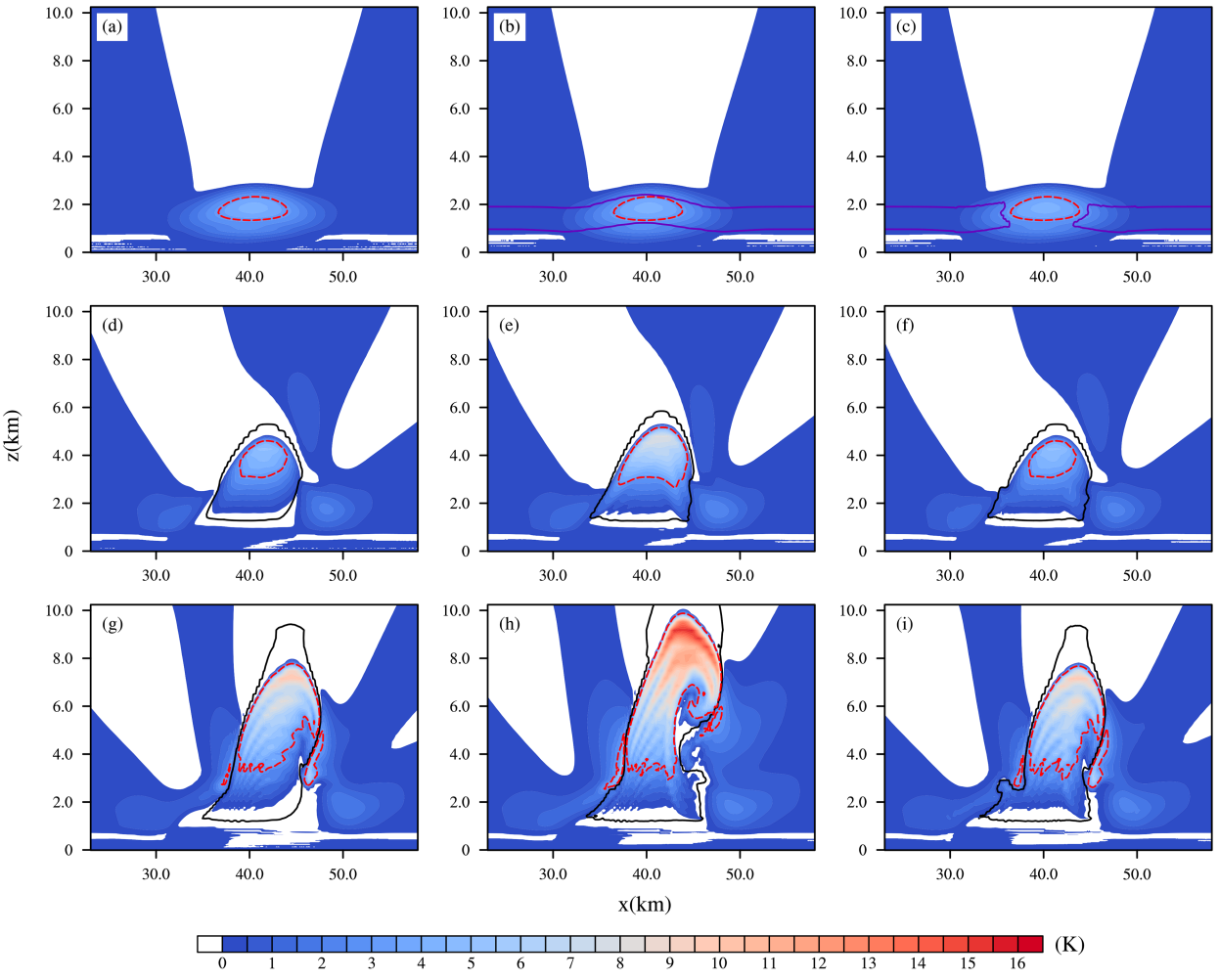

FIG. 11. Vertical cross section of perturbation potential temperature θ' (shaded), the 3.2-K contour of θ' (dashed red), and the 1×10^{-4} kg kg^{-1} contour of cloud water plus cloud ice mixing ratio (solid black) through maximum w for (left) CNTL, (middle) CN_M12, and (right) CN_M12nb at (a)–(c) 200, (d)–(f) 600, and (g)–(i) 900 s of simulations. The solid blue lines in (b) and (c) depict the 0.3 g kg^{-1} q_v differences from CNTL.

CNTL, the maximum w is found near $x = 8$ km, significantly lagging behind the cold pool's leading edge, which is positioned around 11.5 km. This rearward displacement is attributed to stronger tilting of the low-level inflow. At 1800 s, this pattern persists, with the midlevel updraft in CNTL positioned 2.5–5.0 km behind the surface gust front (Fig. 15d). In CN_M12nb, the updraft remains much closer to the gust front and rises nearly vertically up to ~7 km before tilting forward (Fig. 15c). In CNTL, forward tilting begins around 4 km, owing to the weaker w (Fig. 15d).

In CN_M12nb, storm-induced acceleration of the low-level inflow generates a greater near-surface positive shear. In the vertical cross section shown in Fig. 15, approximately 1 km in front of the leading edge of the cold pool, the 0–2-km wind shear in CN_M12nb is ~4 m s^{-1} stronger than the environmental shear and ~3 m s^{-1} stronger than that in CNTL at 1800 s. This shear generates horizontal vorticity oriented into the page and should help support an updraft with less rearward tilt at the lower levels according to the Rotunno–Klemp–Weisman (RKW) theory (Rotunno et al. 1988; Fig. 15c). Another more important reason for the more upright updraft in CN_M12nb is the higher positive buoyancy (maximum $\theta' \sim 10.5$ K in Fig. 15a vs ~7.9 K in CNTL in Fig. 15b) due to the enhanced near-LCL humidity that causes more rapid vertical acceleration of lifted air parcels and larger w, leading to the more vertical parcel trajectories and deeper convection.

By 2200 s, the updraft of right mover in CNTL has become even more rearward tilted at the lower levels, with its leading edge positioned approximately 5 km behind the surface gust front (Fig. 15f). This pattern is consistent with the updraft positioning observed in Fig. 6. In CNTL, the inflow air travels over the gust front but fails to directly connect with the updraft, which is positioned approximately 5 km behind the leading edge of the gust front. During this separation, dilution of buoyancy and moisture may occur. In contrast, the lifted air in CN_M12nb begins to rise immediately behind the

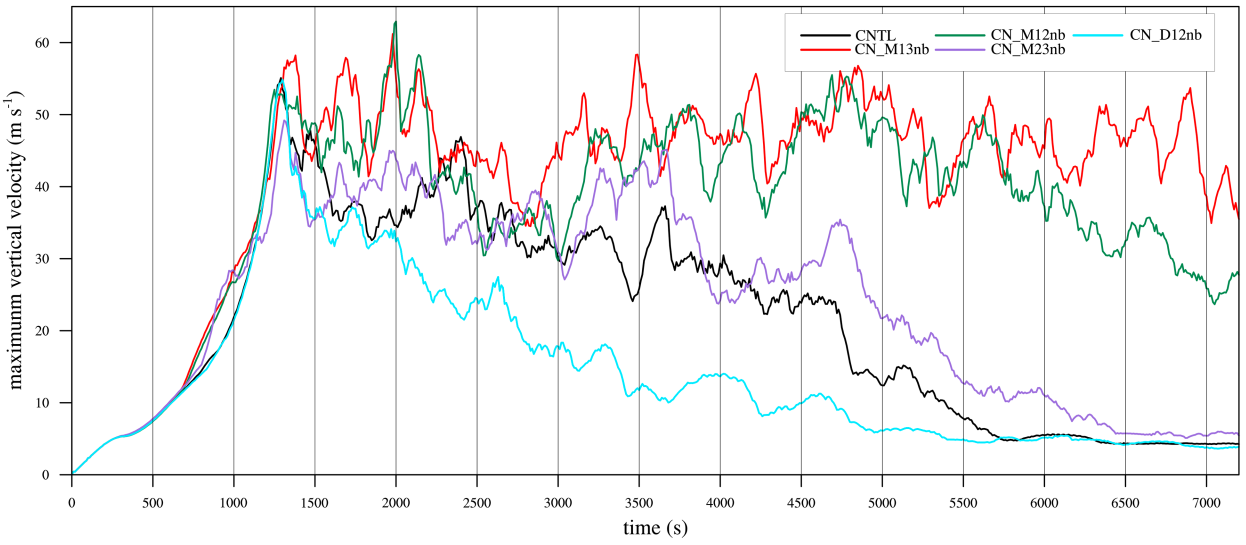

FIG. 12. Time series of maximum vertical velocity for CNTL (black), CN_M13nb (red), CN_M12nb (green), CN_M23nb (purple), and CN_D12nb (light blue).

surface gust front and feeds the main updraft, which is located only about 1 km behind the gust front (see also Fig. 14e). The resulting updraft is notably more upright and deeper, staying much closer to the gust front—a key distinction from CNTL. This behavior is attributed to the enhanced environmental humidity in the 1–2-km layer AGL. The presence of moist layer leads to substantially higher buoyancy within the storm updraft, which we believe is the primary driver of the much more upright updraft. The resulting larger vertical acceleration of the rising air parcels contributes to the steeper slopes of storm updrafts. In addition, the stronger updraft becomes less susceptible to disruption by environmental shear, thereby maintaining a more stable structure. A secondary effect is the enhanced inflow near the surface, where increased horizontal acceleration generates positive shear that further supports upright updrafts in the lower levels.

To better understand how the environmental moisture near the cloud base affects the updraft buoyancy and subsequently impacts storm evolution, we calculate water vapor entrainment using the method described in section 2d. During the initial stage (before 900 s), the total water vapor entrainment into the storm updrafts is similar across the simulations. However, as the storm develops, notable differences in both entrainment and updraft buoyancy emerge.

Figure 16 presents the time series of total water vapor entrainment (entrainment for short) into the updraft cores (defined by $w > 2$ m s^{-1}), the entrainment normalized by the updraft volume, and the updraft volume itself, over the 1210–1980 s period for CNTL, CN_M13nb, CN_M12nb, CN_M23nb, and CN_D12nb experiments. This period starts shortly before the first w_{max} peak and ends when the initial storm starts to split but already exhibits sufficient difference in intensity (Fig. 12). The selection of this period makes our computation easier by not having to track separate cells after splitting. At even later times, storms in CNTL become much weaker after splitting, making direct quantitative comparisons across experiments difficult. A similar analysis was also conducted for the 1630–2400-s period, and the results obtained are similar (not shown).

Figure 16a shows that the total entrainment in CN_M13nb and CN_M12nb is greater than in the other simulations throughout the entire 12-min period. The updraft core volumes in CN_M13nb and CN_M12nb are also larger (Fig. 16c). The larger volume is associated with stronger updrafts in our simulations and reflects an expanded interface for entraining ambient moisture. Figure 16b shows the total entrainment normalized by the total updraft core volume. The normalized entrainment values in CN_M13nb and CN_M12nb remain consistently higher than those in others and are still similar to each other.

The continuous entrainment of high-humidity air into the updraft core supports the sustained development of storms. The time-integrated entrainment values are presented in Fig. 17. The CN_M12nb and CN_M13nb exhibit similarly larger time-integrated total entrainment (TITE), and both experiments produced the longest-lived and most intense supercells. In comparison, CN_M23nb and CNTL exhibit similar but notably lower TITE than CN_M12nb and CN_M13nb, corresponding to short-lived storms. Last, CN_D12nb, with the lowest TITE, only generates the weakest and shortest-lived storm. The differences among the normalized TITE values across the various experiments mirror those observed in the absolute TITE values, albeit with reduced magnitude. These differences in moisture entrainment govern the buoyancy intensity within the updraft core, as measured by θ'_{max} within the updraft (Fig. 17c). The θ'_{max} is on average 2–3 K higher in CN_M12nb and CN_M13nb, and this increased buoyancy produces stronger and more upright updrafts as discussed earlier. The results also show that enhancing moisture in the 2–3-km layer AGL does not lead to increased entrainment into the updraft core compared to CNTL.

Evidently, at least among the scenarios considered here, moisture in the 1–2-km layer AGL plays a critical role in supercell evolution. Weak and short-lived storms can change

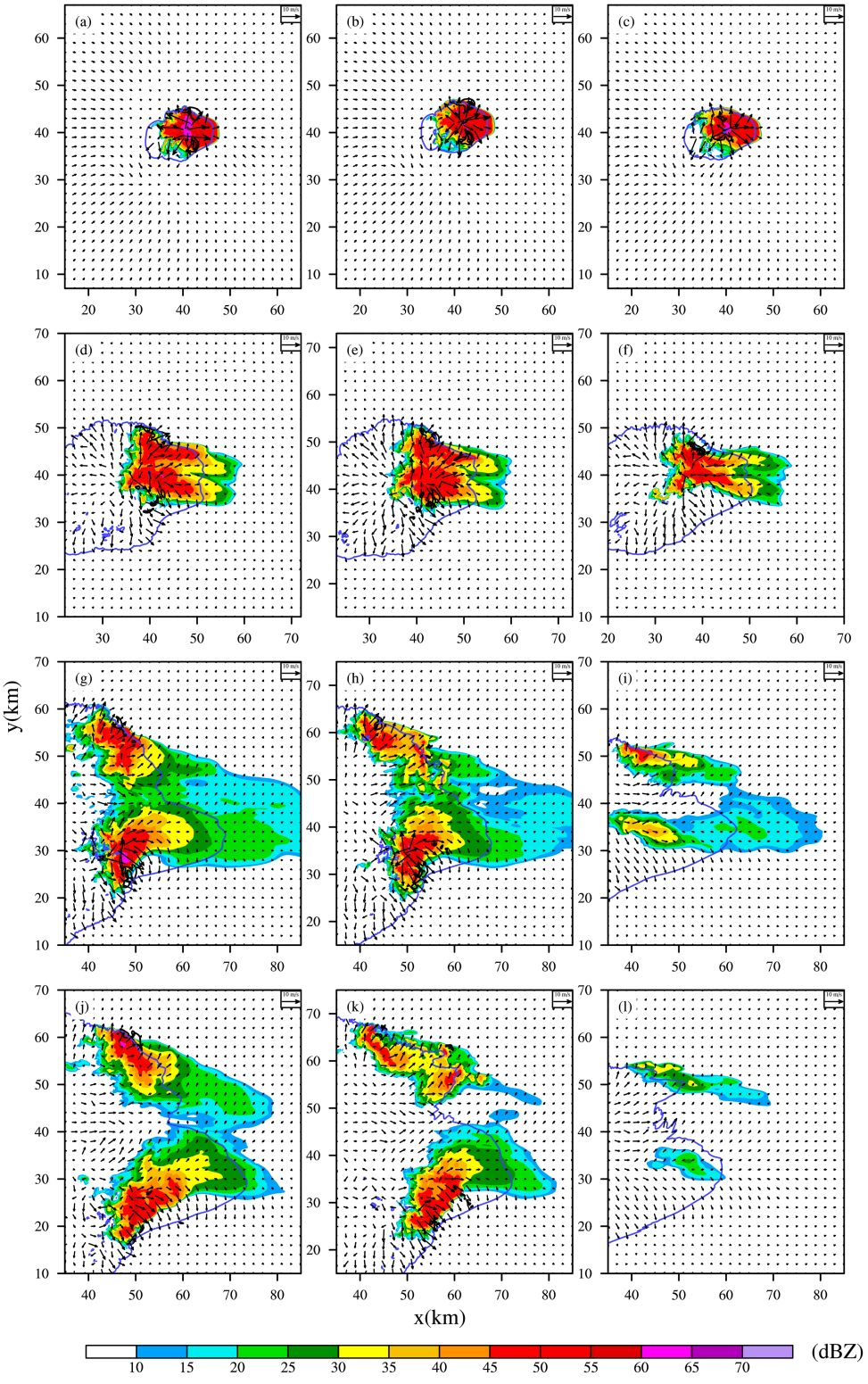

FIG. 13. As in Fig. 6, but for (left) CN_M13nb, (middle) CN_M12nb, and (right) CN_M23nb at (top)–(bottom) 1800, 3000, 5400, and 6400 s.

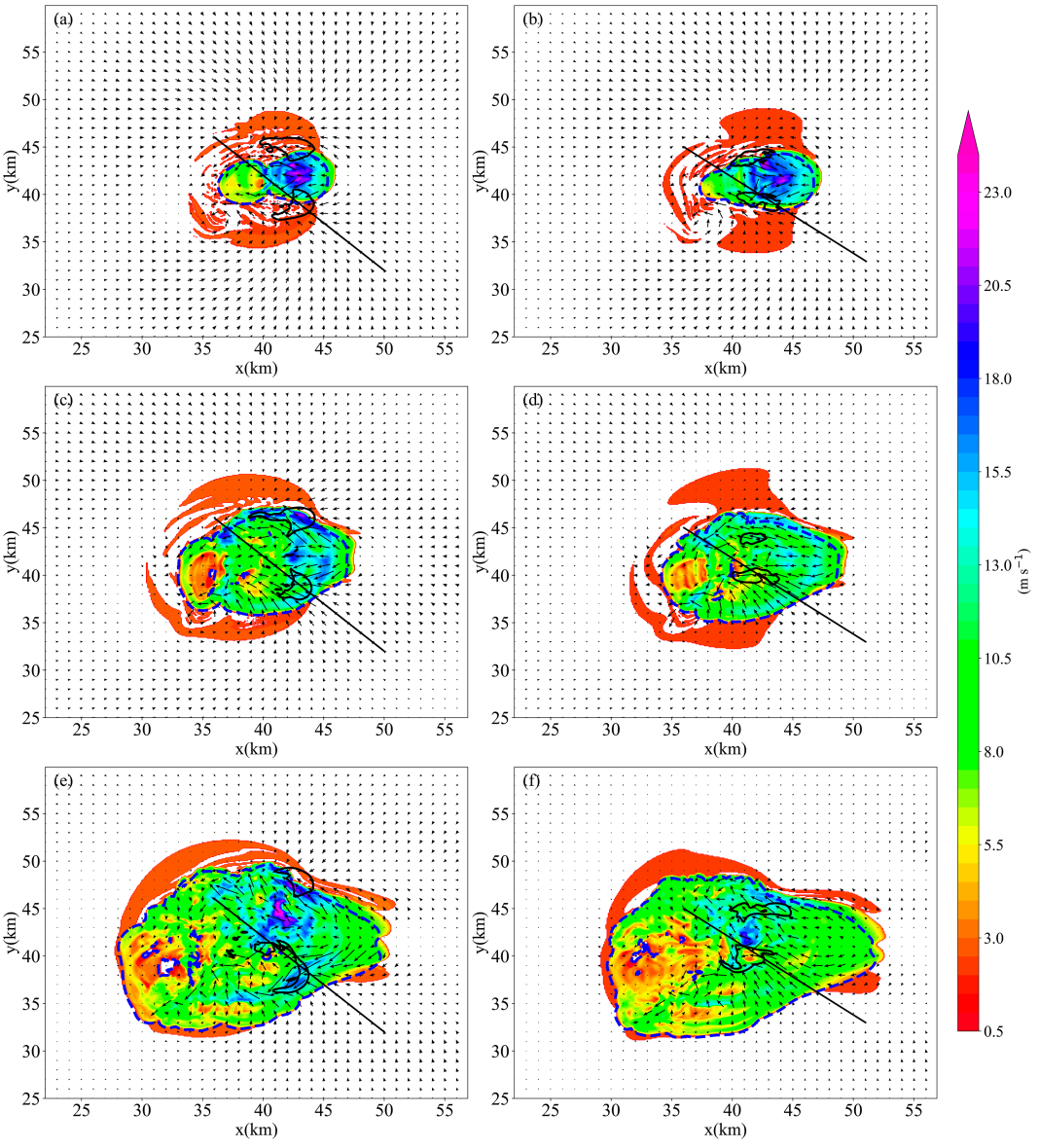

FIG. 14. Cold pool strength parameter C (shaded), -1-K θ' contour (dashed blue line) at 10 m AGL, and 10 m s^{-1} w contour (solid black line) at 3125 m AGL and perturbation wind vectors at 959 m AGL for (left) CN_M12nb and (right) CNTL at (top) 1500, (middle) 1800, (bottom) and 2200 s. The perturbation wind is defined as departure from the base-state wind. The black straight solid lines through the right movers represent the locations of vertical cross sections in Fig. 15.

into strong, long-lived supercells when this layer is moistened, due to increased environmental water vapor entrainment. Notably, moisture change in this layer have minimal impact on traditional thermodynamic parameters such as LCL or CAPE. This suggests that severe weather forecasting based on environmental conditions should place greater emphasis on fine-scale structures in thermodynamic profiles, in particular, moisture near the cloud base.

In the following, we examine further process differences between CNTL and CN_M12nb. Vertical profiles of total water vapor entrainment averaged over 60-s periods are shown in Fig. 18 for the two simulations. At earlier times (1210–1270 s and 1330–1390 s), the strongest enhancement of entrainment in CN_M12nb occurs within the 1–2 km AGL (Figs. 18a,b). During this stage, the storm updrafts triggered by the initial bubble have just reached their first peak (see Fig. 12), while downdrafts and cold pool are still in the process of developing. The entrainment values are largest near the LCL for both CNTL and CN_M12nb, indicating that most upward water vapor inflow below the LCL (mostly upward), along with some side entrainment above the LCL, serves as the primary source of storm moisture supply. The compensating downdraft

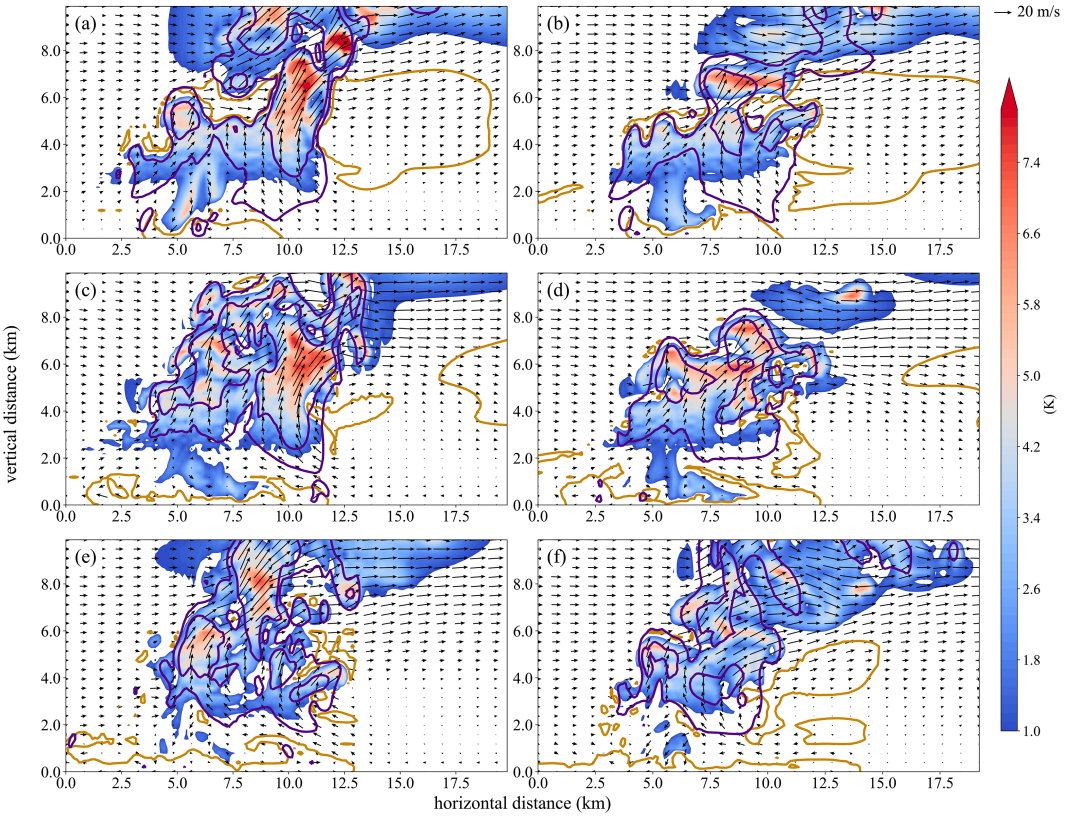

FIG. 15. Vertical cross section along the black straight solid lines in Fig. 14 for (left) CN_M12nb and (right) CNTL at (top) 1500, (middle) 1800, and (bottom) 2200 s of θ' (positive values shaded) with the −1-K contours (solid golden, indicating the boundaries of cold pool), 5 and 13 m s^{-1} w contours (solid purple), and ground-relative wind vectors. Note that the color scale differs from that used in Fig. 11.

surrounding the updraft can also transport some environmental moisture downward and subsequently into the updraft. As the storm further develops, precipitation begins to fall, initiating downdrafts and forming surface cold pool that spread at the surface. The resulting gust fronts on all sides of the cold pool lifts lower-level air (cf. Fig. 15c), which then feeds the updraft, leading to a substantial water vapor entrainment at lower levels (below 1 km, Figs. 18d–f). Around 1800 s, there is a local maximum entrainment in CN_M12nb at ~2.3-km level that is absent in CNTL (Figs. 18e,f). The analysis of vertical cross sections of wind (e.g., Fig. 15c) and water vapor fields suggests that this feature arises primarily from the elevation of the ~1-km moist layer by the flows lifted by the spreading cold pool on the back side of the low-level flow. The more important general tendency is for a deeper layer of strong entrainment to be developed that extends from the surface to above LCL as the storm matures.

Next, we examine the evolution of moisture, temperature, and buoyancy along air parcel trajectories ending in the peak updrafts of CN_M12nb and CNTL. We calculate backward trajectories terminating at the grid point corresponding to w_{max} (referred to as "peak w point") and eight points around it. The eight points are at the center of the four sides and at the four corners of a 500 m × 500 m square centered on the peak w point. For each experiment, the trajectories are traced from the peak w region at two times: 1640 and 1990 s for CN_M12nb and 1750 and 1960 s for CNTL (see Fig. 12), and the trajectories are traced backward in time to 300 s. The slightly different timing of peak w_{max} between the two simulations is chosen to enable a more equitable comparison by aligning the respective stages of storm evolution.

We find that, in CN_M12nb, the air parcels contributing to the peak updraft at both 1640 and 1990 s primarily originate from the humidified 1–2-km layer (Figs. 19b,d). In both CN_M12nb and CNTL, these air parcels first experience a period of descent, followed by horizontal advection, before ascending vertically into the updraft (Figs. 19a,b,d). It is evident that these parcels are driven by the circulation associated with the horizontal vorticity, which is mainly generated baroclinically by the horizontal buoyancy gradients (Markowski and Richardson 2010). However, the initial altitudes of these parcels in CNTL are slightly lower than those in CN_M12nb, with most of them below 1 km AGL.

The average buoyancy (including water loading), q_v, θ', and RH of these two sets of air parcels along their trajectories are calculated (1750 s in CNTL vs 1640 in CN_M12nb and 1960 s in CNTL vs 1990 s in CN_M12nb). Given the varying heights of parcels at the same time steps, all variables are interpolated

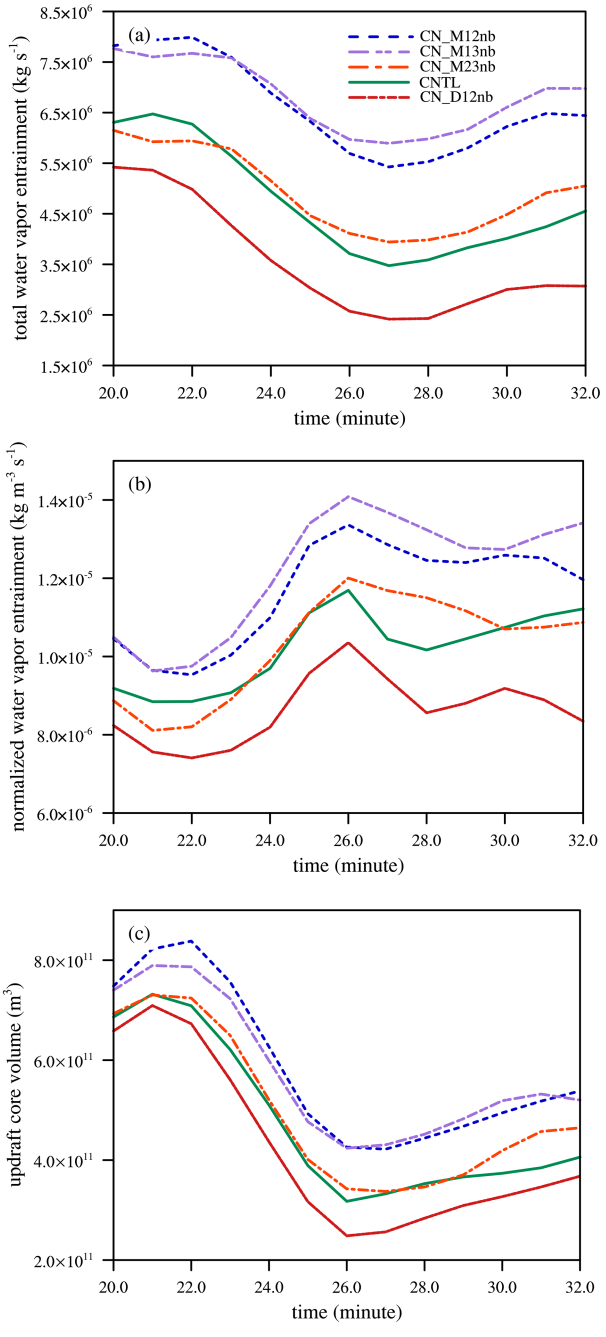

FIG. 16. Time series of (a) total water vapor entrainment, (b) normalized water vapor entrainment, and (c) updraft core volume for CN_M13nb (dashed purple), CN_M12nb (dashed blue), CNTL (solid green), CN_M23nb (dashed orange), and CN_D12nb (dashed red).

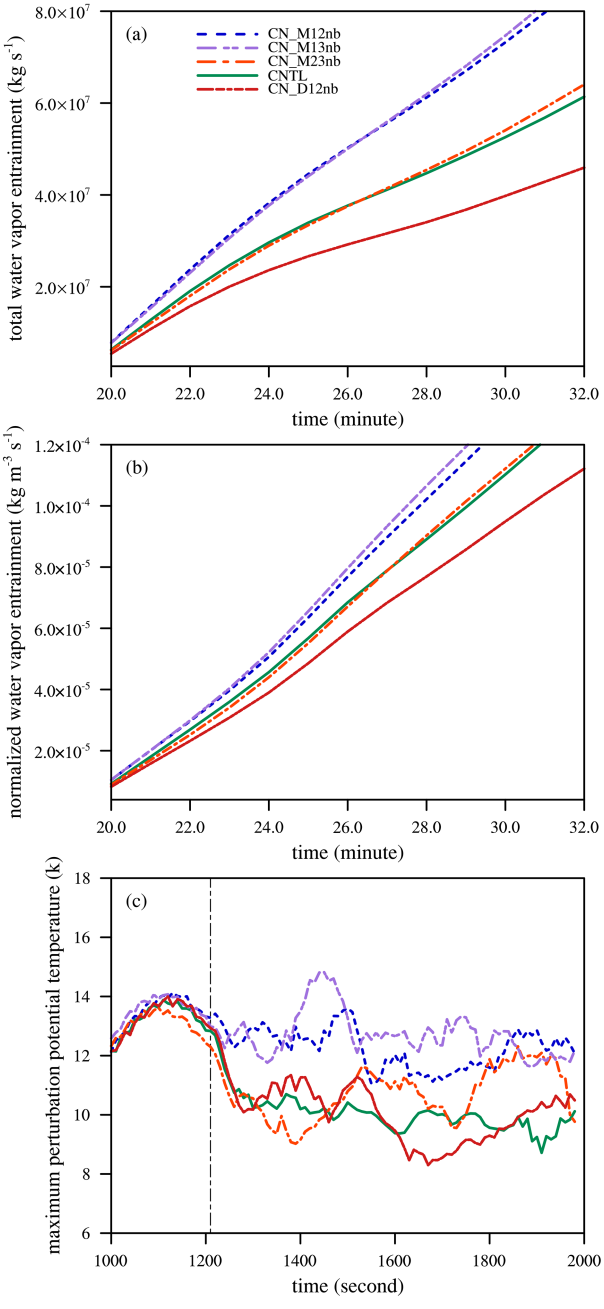

FIG. 17. Evolution of (a) time integral of total water vapor entrainment, (b) time integral of normalized water vapor entrainment, and (c) maximum perturbation potential temperature (θ'_{max}) for CN_M13nb (dashed purple), CN_M12nb (dashed blue), CNTL (solid green), CN_M23nb (dashed orange), and CN_D12nb (dashed red). The vertical dashed line in (c) indicates the start of the period for entrainment calculation (1210 s), which is also the point at which θ'_{max} begins to differ among the simulations.

to common altitude levels to facilitate averaging at each time interval. Additionally, the parcels whose trajectories deviate substantially from the group mean are excluded from the averages, such as the one originating near 6-km height in Fig. 19a. Due to the similarity in the outcomes of the two sets of trajectory diagnostics, only the results of the second set are presented (1960 s in CNTL vs 1990 s in CN_M12nb, Fig. 20). It is evident that the average q_v of air parcels in CN_M12nb is consistently higher than in CNTL throughout the vertical profile. The increased moisture results in saturation

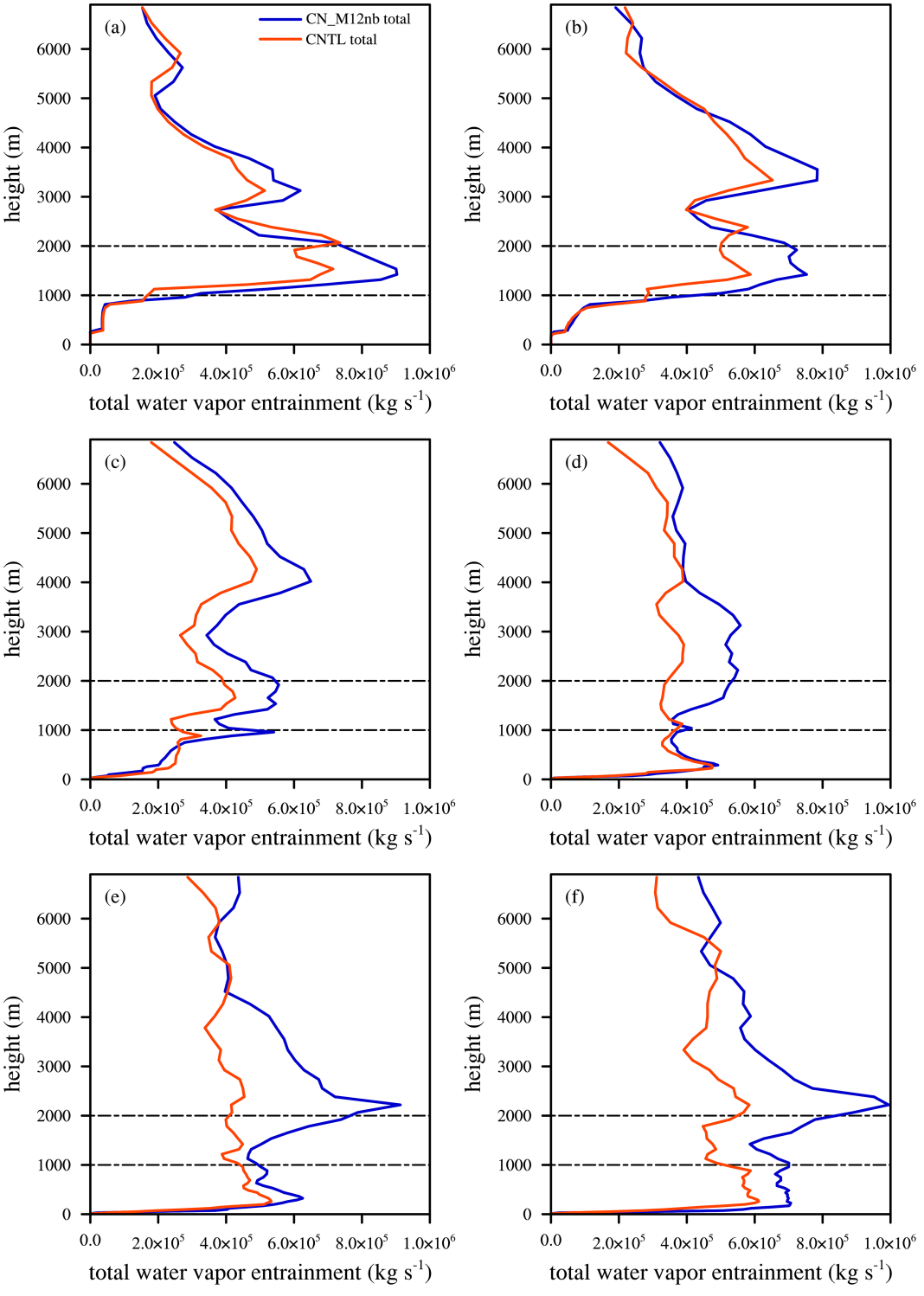

FIG. 18. Vertical profiles of total water vapor entrainment averaged over 60-s periods for CNTL (solid orange) and CN_M12nb (solid blue) at (a) 1210–1270, (b) 1330–1390, (c) 1450–1510, (d) 1630–1690, (e) 1750–1810, and (f) 1870–1930 s. The two dashed black lines at the height of 1000 and 2000 m denote the range of moistened layer for CN_M12nb.

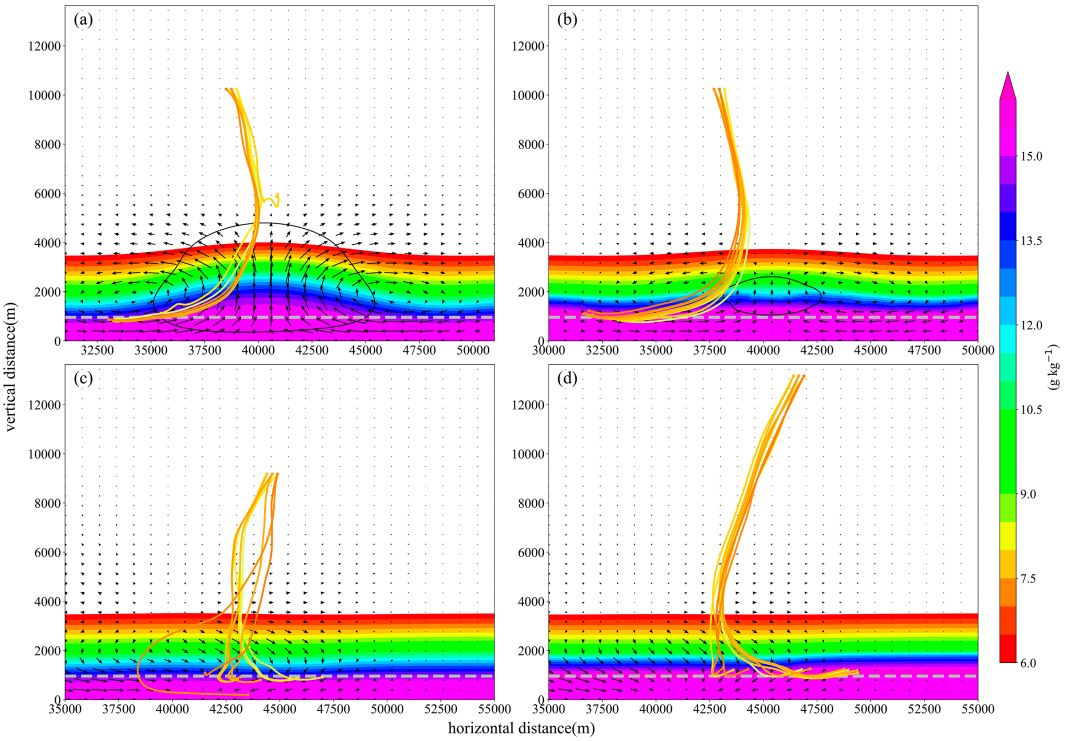

FIG. 19. Vertical cross sections of trajectories of air parcels from 300 s to (a) 1750 s and (c) 1960 s for (left) CNTL and to (b) 1640 s and (d) 1990 s for (right) CN_M12nb, water vapor specific humidity (shaded), and perturbation wind vectors at 300 s. The solid black lines in (a) and (b) depict the 1.0 m s^{-1} vertical velocity isopleth. The thick dashed gray line represents the location of the bottom (1 km AGL) of the moistened layer in CN_M12nb. The cross sections of (a) and (b) are *Y*–*Z* plane and of (c) and (d) are *X*–*Z* plane to better display the trajectories of nine air parcels (represented by lines of different colors) of each diagram. The position of the *Y*–*Z* plane on the *x* axis is equal to the *X* position of the corresponding peak point, and the position of the *X*–*Z* plane on the *y* axis is equal to the *Y* position of the corresponding peak point.

(average RH close to 100%) at lower altitudes. The enhanced water vapor leads to θ' that is typically 1–2 K higher throughout the depth (Fig. 20b) and higher positive buoyancy (Fig. 20a) in CN_M12nb. The somewhat lower buoyancy in CN_M12nb between 5 and 6 km in Fig. 20b may be due to enhanced water loading as θ' is clearly higher (Fig. 20b). The accumulative effect of larger positive buoyancy along the parcel trajectories above 1 km naturally leads to a much stronger updraft and larger w_{max} peaks in CN_M12nb. These differences are attributable solely to the enhanced environmental humidity entrained into the updraft core.

f. Sensitivity to initial bubble configurations

Before 1800 s, the simulations remain strongly influenced by the initial thermal bubble. A natural question arises: How sensitive are the results to configuration of this initial bubble? To address this, we conducted a series of additional sensitivity experiments with varied bubble configurations. First, we repeated experiments CNTL and CN_M12nb with the maximum warm bubble perturbation reduced to 3 K, referred to as CNTL_3K and CN_M12nb_3K, respectively. Although the overall storm intensity is weaker in these runs, the storm longevity remains generally consistent with that in 6-K bubble cases. The storms in CNTL_3K still fail to sustain. While the cold pool associated with the right-moving storm is weaker in both spatial extent and intensity, it still propagates too fast, cutting off the warm and moist inflow necessary to maintain the updraft. In contrast, the storms in CN_M12nb_3K remain persist, similar to those in CN_M12nb (results not shown).

Variations in the height of the initial bubble may alter the altitude of the compensating circulation associated with the initial updrafts, potentially affecting the entrainment process. To assess whether the level of maximum entrainment is sensitive to the height of the initial bubble, we repeated CN_M12nb with the bubble centered at a higher altitude of 2500 m (hereafter CN_M12nb_hb, where "hb" denotes higher bubble). The overall storm intensity remains largely unchanged, particularly during the latter stages of storm development (results not shown). Compared to CN_M12nb, there is a slight upward shift in the height of the maximum entrainment layer in CN_M12nb_hb storms; however, this difference is limited to the first 30 min. As the system gradually stabilizes, the influence of the initial thermal bubble diminishes, leading to essentially same vertical distributions of entrainment between CN_M12nb and CN_M12nb_hb. The entrainment profiles closely resembles the pattern depicted in Figs. 18e and 18f, with the maximum water

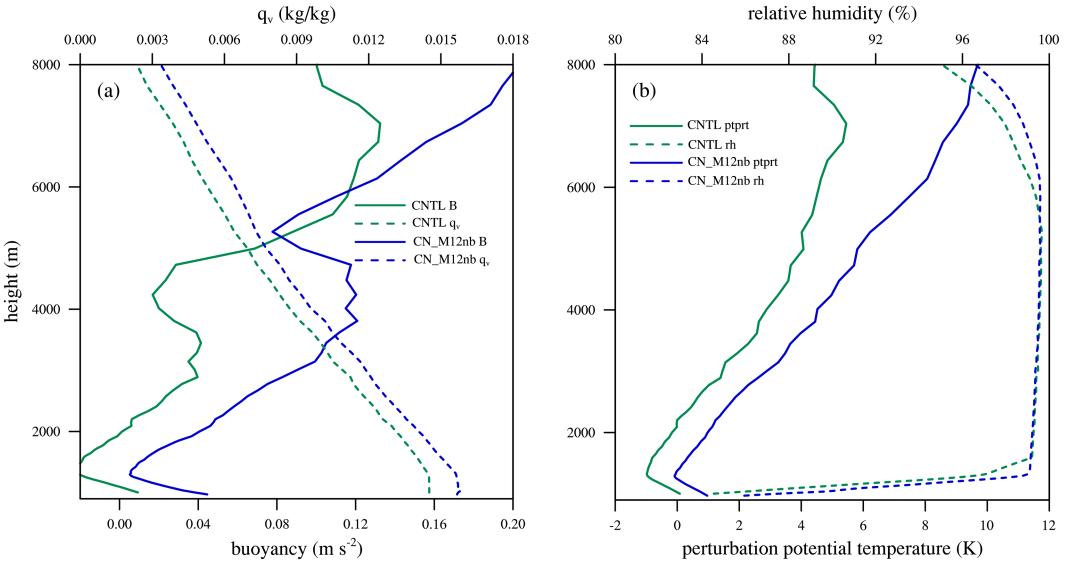

FIG. 20. (a) Average buoyancy and q_v along the trajectories of CNTL trajectories in Fig. 19c and CN_M12nb trajectories in Fig. 19d. (b) As in (a), but for average perturbation potential temperature and RH. The variables of different particles from CNTL and CN_M12nb have been interpolated to the same height at each time point in these four subplots. Only the part with ascending motion is included.

vapor entrainment occurring near 2 km and a substantial amount entrainment observed below 1 km (results not shown).

Given that the right-moving storms in CN_M12nb and CN_M12nb_hb are similarly sustained, we compared moisture entrainment between 2830 and 3600 s. The height of the maximum water vapor entrainment layer is found to be nearly identical in the two simulations (results not shown), indicating the general results are not sensitive to the initial bubble height.

Recent studies (e.g., Peters et al. 2020) have shown that simulated storms are often sensitive to the updraft width, which can be linked to the initial bubble size. Peters et al. (2022a,b) specifically investigated the relationship between convection initiation and environmental wind shear, exploring how updrafts evolve under varying initial forcing radius in different wind shear, humidity, and CAPE conditions. Their experiments considered initial bubble radii up to 3 km. Since our experiments use a 10-km horizontal radius, the bubble should be sufficiently large to eliminate the updraft width as the cause of early storm demise (due to dry air entrainment). Our results are consistent with the findings of Peters et al. (2022b), that for environments characterized by lower humidity, neither increasing the initial radius nor enhancing wind shear is sufficient to produce a stable, self-sustaining state of updrafts (see their Figs. 2e,k). Nevertheless, we repeated CNTL with an increased horizontal radius of 15 km, referred to as CNTL_wb ("wb" denoting wider bubble). The simulated storm remains short-lived, although the maximum updraft maintains its intensity for longer (up to 4000 s, results not shown), due to its increased initial buoyancy energy and less dry air entrainment, as pointed out in Peters et al. (2020).

4. Summary and conclusions

This study conducts a series of tornadic supercell simulations based on a composite sounding and its variations for significant tornadoes in China. Using a high-resolution model with a horizontal grid spacing of 100 m, the simulation initialized with the original composite sounding yielded only short-lived, unsustainable storms. Relatively weak vertical wind shear and lower SRH were initially suspected to be responsible, but enhancing them did not improve storm longevity; in fact, stronger wind shear resulted in weaker simulated storms. Furthermore, even though the original and modified hodographs had clockwise curvature at the lower levels, the left mover after the storm splitting was stronger than the right mover (e.g., CNTL, CN_Vx2sl), and the significant lagging of the right mover behind the surface gust front was a prominent feature in the unsustainable storm simulations.

Through a series sensitivity experiments, we found that enhancing the RH in the 1–2-km layer AGL alone—from ~83% in the original composite sounding to ~94%—led a substantial change in storm evolution. The overall system became long-lived, and the right-moving supercell after splitting became stronger than the left mover, consistent with expectations for a hodograph having clockwise curvature. Moisture enhancement primarily occurs in a layer just above yet close to, the LCL, influencing storms through a downward-then-upward transport of moisture into the storm updraft, as driven by compensating circulations around low-level updrafts in the early stage. This mechanism differs from direct increases in subcloud-layer moisture. The moisture enhancement within the 1–2-km layer AGL has minimal impact on the calculated LCL or CAPE, making severe storm forecasting based on mixed layer or surface-based thermodynamic parameters

tricky. This finding also underscores the important impacts of fine-scale variations in environmental soundings, which are not adequately captured by commonly used parameters.

Specifically, in a set of sensitivity experiments—CN_M12nb, CN_M13nb, and CN_M23nb—the RH in the 1–2-, 1–3-, and 2–3-km layers AGL is increased, respectively. In CN_D12nb, RH in the 1–2-km layer AGL is decreased. The most notable differences in storm morphology among these simulations lie in the behavior of the split storms. In CN_M12nb and CN_M13nb, both the right and left movers remain close to the cold pool outflow gust fronts, with the right mover intensifying. In contrast, in CN_M23nb, CNTL, and CN_D12nb, the right mover is located far (as much as 10 km) from its rear-flank gust front and is weaker than the left mover. Storm intensity is sustained throughout the 2-h simulations in the former group but declines in the latter, suggesting that close proximity between the storm and its associated gust front is essential for maintaining storm longevity.

In those long-lived supercells, the storms remain near the cold pool gust fronts primarily due to stronger updrafts, which are driven by substantially enhanced positive buoyancy resulting from increased moisture in the 1–2-km layer AGL. The more vigorous updrafts induce stronger low-level inflow, which slows the advancement of the more intense cold pool associated with enhanced precipitation. More importantly, the enhanced vertical acceleration causes the air parcels to rise more rapidly than the short-lived cases, and also, the rise is more than the horizontal rearward drift of the parcels. As a result, both steeper slope of the updraft and the comparable propagation of cold pool contribute to keep the updraft closer to the low-level gust front in the long-lived cases. Additionally, the stronger low-level storm-relative inflow in these cases can acquire additional positive shear to offset the negative shear produced at the cold pool gust front, promoting a more upright low-level updraft based on the RKW theory (Rotunno et al. 1988).

Calculation of the total water vapor entrainment into updraft cores reveals that long-lived supercells entrain more environmental moisture than short-lived storms. The enhanced entrainment leads to greater latent heat release, resulting in stronger positive buoyancy that supports more intense, deeper, and more upright updrafts throughout the 2-h simulations. The failure in obtaining sustained storms in CN_M23nb when RH in the 2–3-km layer is increased is attributed to water vapor entrainment rates comparable to those in CNTL. These results emphasize the pivotal role of ambient humidity near the cloud base—a factor often overlooked in previous studies—whereas moisture enhancement at higher levels, such as 2–3 km AGL, sometimes fails to positively influence storm development. Additionally, unlike previous studies that calculate the entrainment of environmental air mass (without the water vapor component), our entrainment calculations, using a new procedure developed, directly quantify water vapor entrainment flux into storm updrafts, offering a more accurate measure of moisture intake. By incorporating fluxes entering from below the cloud base, the calculation provides a more complete representation of moisture budget.

Vertical profiles of the total entrainment into the updrafts show that the greatest water vapor entrainment occurs near and just above the cloud base at the earlier stage of storm development (~20 min into the simulations). At this stage, moist environmental air is drawn into the base of the updraft by compensating downdrafts surrounding it. As the storm matures and the cold pool develops, strong moisture entrainment extends downward to near the surface as the low-level inflows are lifted by the gust fronts. Large entrainment can also extend upward above the cloud base level as low-level air is elevated by the spreading cold pool before entering the updraft.

To further illustrate the differences in updraft parcel properties, total buoyancy, q_v, θ', and RH of air parcels are calculated along trajectories traced back from peak w_{max} locations. In CN_M12nb, with enhanced 1–2-km moisture, parcel q_v and θ' are both higher than in CNTL, and buoyancy is greater at most levels, further confirming our conclusion that moisture near the cloud base substantially influences updraft strength.

Our findings partially align with the results of JLT23, which reported that reduced humidity at 3–4 km leads the storm-relative airstream to entrain drier low-level air into the storm core, resulting in a decline in buoyancy, vertical mass flux, and precipitation within the storm. Complementarily, our study emphasizes the importance of updraft–cold pool interactions, showing that the proximity of the updraft to cold pool gust front is critical for its maintenance. Moisture variations within a thin layer near cloud base not only modulate storm intensity but also, more importantly, govern the ability of storms to persist by affecting this interaction.

One factor closely linked to cold pool characteristics is the microphysics scheme used, as discussed in the introduction. Different schemes can lead to significant variations in cold pool intensity and structure (Dawson et al. 2010). Given the critical role of updraft–cold pool interaction in storm development, the influence of microphysics schemes cannot be overlooked. Further investigations using, e.g., more sophisticated multimoment ice microphysics schemes are warranted.

In conclusion, this study demonstrates a pronounced sensitivity of simulated storms to moisture in a shallow layer just above the LCL and provides explanations for such behaviors from several perspectives. Importantly, it may not be the absolute altitude of the dry or moist layer that governs storm evolution but rather its position relative to the LCL or cloud base. This relative positioning influences the level at which substantial environmental air is entrained into the updraft through the down-in-up process by the compensating circulation—a key process highlighted in this study.

Future work should explore a broader parameter space, including background environments with varying moisture content and CAPE, as well as hodographs with differing magnitudes of low-level shear and SRH. The fact that the low-level hodograph curvature seems to have a more significant role to play when the split cells can maintain their inMarkowski 2024tensity but not so in the opposite situation is worth studying, from the dynamic versus thermal buoyancy forcing point of view. Furthermore, some studies, including Markowski and Bryan (2016) and Markowski (2024), have emphasized the importance of explicitly excited (by introducing initial thermal perturbations into the boundary layer) turbulent eddies in well-mixed boundary layer that is typical of the environmental soundings used in

most supercell simulation studies. Markowski (2024) found that vertical vorticity streaks developing in such turbulent boundary layer can alter the way tornado-like vortices form in supercell simulations. How such boundary layer eddies may influence the moisture entrainment into simulated supercells, as studied in this paper, is also worth studying in the future.

Acknowledgments. This work was primarily supported by NSFC Grant 41730965.

Data availability statement. The final dataset used in this paper is available from Harvard Dataverse at https://doi.org/10.7910/DVN/ATRUMD.

APPENDIX

Spinup Procedure to Obtain Sounding Wind Profile in Geotriptic Balance

Writing the horizontal pressure gradient forces in terms of the geostrophic wind components U_g and V_g, the momentum equations are

$$\frac{\partial U}{\partial t} = f(V - V_g) + F_x, \tag{A1}$$

$$\frac{\partial V}{\partial t} = -f(U - U_g) + F_y, \tag{A2}$$

where U and V are the horizontal wind components and f is the Coriolis parameter. The F_x and F_y are the components of frictional force that contain the surface drag at the surface. The horizontal advection terms are neglected assuming the base-state environment is horizontally homogeneous. When the three terms on the right-hand side are in balance, the time tendencies go to zero. Following R16, we arrive at the (U, V) profile by running the ARPS model in a one-dimensional (1D) column mode to a steady state with the same model configurations as the 3D storm simulations. For that, we need to specify geostrophic wind profile (U_g, V_g). In R16, the initial wind profile, extracted from a real-data simulation of a tornado outbreak, was assumed to be in geostrophic balance, which is not necessarily appropriate because the lower layers of this profile already include surface drag. Thus, we estimate (U_g, V_g) from the horizontal pressure gradient in the ERA5 dataset, as shown by the green dotted–dashed line in Fig. 1b. In R16 and Dawson et al. (2019), the geostrophic wind is assumed to be equal to the initial wind profile so the amount of spinup adjustment is small and a quasi-steady state can be achieved. In our case, due to the significant difference between the initial wind profile of OCS (black solid line in Fig. 1b) and the geostrophic wind profile (green dashed–dotted line in Fig. 1b), large oscillations around the geostrophic wind are found away from the ground in the spinup simulation that do not settle with time, apparently due to the lack of significant frictional damping at those levels. To avoid this issue, we choose to use the geostrophic wind profile as the initial input instead for the spinup process, which will be adjusted near surface in response to the surface drag. It is clear that the frictional effect is primarily confined to below 1 km. Our setup is actually similar to that of Markowski (2020, see his Fig. 1b) where his initial wind profile (assumed geostrophic) is a straight hodograph similar to our geostrophic wind profile, and the final profile has curvature similar to our final curved hodograph (red dashed line in Fig. 1b). The low-level SRH of the final profile is comparable to that of the original OCS, although it underrepresents the jet-like ageostrophic feature near 1-km level. Because the main focus of this study is on moisture sensitivity, given the particular environmental wind profile in the presence of surface drag, maintaining the original profile of OCS is not critical for our purpose. Future studies can try to test the main conclusions of this paper using a final profile close to that of OCS.

REFERENCES

Brown, R. G., and C. Zhang, 1997: Variability of midtropospheric moisture and its effect on cloud-top height distribution during TOGA COARE. *J. Atmos. Sci.*, **54**, 2760–2774, https://doi.org/10.1175/1520-0469(1997)054<2760:VOMMAI>2.0.CO;2.

Bunkers, M. J., 2002: Vertical wind shear associated with left-moving supercells. *Wea. Forecasting*, **17**, 845–855, https://doi.org/10.1175/1520-0434(2002)017<0845:VWSAWL>2.0.CO;2.

——, M. R. Hjelmfelt, and P. L. Smith, 2006: An observational examination of long-lived supercells. Part I: Characteristics, evolution, and demise. *Wea. Forecasting*, **21**, 673–688, https://doi.org/10.1175/WAF949.1.

Burgess, D. W., 1976: Single Doppler radar vortex recognition: Part I—Mesocyclone signatures. *17th Conf. on Radar Meteorology*, Seattle, WA, Amer. Meteor. Soc., 97–103.

Chavas, D. R., and D. T. Dawson II, 2021: An idealized physical model for the severe convective storm environmental sounding. *J. Atmos. Sci.*, **78**, 653–670, https://doi.org/10.1175/JAS-D-20-0120.1.

Coffer, B. E., and M. D. Parker, 2017: Simulated supercells in nontornadic and tornadic VORTEX2 environments. *Mon. Wea. Rev.*, **145**, 149–180, https://doi.org/10.1175/MWR-D-16-0226.1.

——, ——, R. L. Thompson, B. T. Smith, and R. E. Jewell, 2019: Using near-ground storm relative helicity in supercell tornado forecasting. *Wea. Forecasting*, **34**, 1417–1435, https://doi.org/10.1175/WAF-D-19-0115.1.

——, ——, J. M. Peters, and A. R. Wade, 2023: Supercell low-level mesocyclones: Origins of inflow and vorticity. *Mon. Wea. Rev.*, **151**, 2205–2232, https://doi.org/10.1175/MWR-D-22-0269.1.

Davies-Jones, R., 1984: Streamwise vorticity: The origin of updraft rotation in supercell storms. *J. Atmos. Sci.*, **41**, 2991–3006, https://doi.org/10.1175/1520-0469(1984)041<2991:SVTOOU>2.0.CO;2.

Dawe, J. T., and P. H. Austin, 2011a: Interpolation of LES cloud surfaces for use in direct calculations of entrainment and detrainment. *Mon. Wea. Rev.*, **139**, 444–456, https://doi.org/10.1175/2010MWR3473.1.

——, and ——, 2011b: The influence of the cloud shell on tracer budget measurements of LES cloud entrainment. *J. Atmos. Sci.*, **68**, 2909–2920, https://doi.org/10.1175/2011JAS3658.1.

Dawson, D. T., M. Xue, J. A. Milbrandt, and M. K. Yau, 2010: Comparison of evaporation and cold pool development between single-moment and multimoment bulk microphysics schemes in idealized simulations of tornadic thunderstorms. *Mon. Wea. Rev.*, **138**, 1152–1171, https://doi.org/10.1175/2009MWR2956.1.

——, B. Roberts, and M. Xue, 2019: A method to control the environmental wind profile in idealized simulations of deep convection with surface friction. *Mon. Wea. Rev.*, **147**, 3935–3954, https://doi.org/10.1175/MWR-D-18-0462.1.

Droegemeier, K. K., S. M. Lazarus, and R. Davies-Jones, 1993: The influence of helicity on numerically simulated convective storms. *Mon. Wea. Rev.*, **121**, 2005–2029, https://doi.org/10.1175/1520-0493(1993)121<2005:TIOHON>2.0.CO;2.

Fischer, J., and J. M. L. Dahl, 2022: Transition of near-ground vorticity dynamics during tornadogenesis. *J. Atmos. Sci.*, **79**, 467–483, https://doi.org/10.1175/JAS-D-21-0181.1.

Flournoy, M. D., and E. N. Rasmussen, 2023: The influence of convection initiation strength on subsequent simulated supercell evolution. *Mon. Wea. Rev.*, **151**, 2179–2203, https://doi.org/10.1175/MWR-D-22-0069.1.

Gilmore, M. S., and L. J. Wicker, 1998: The influence of midtropospheric dryness on supercell morphology and evolution. *Mon. Wea. Rev.*, **126**, 943–958, https://doi.org/10.1175/1520-0493(1998)126<0943:TIOMDO>2.0.CO;2.

Grant, L. D., and S. C. van den Heever, 2014: Microphysical and dynamical characteristics of low-precipitation and classic supercells. *J. Atmos. Sci.*, **71**, 2604–2624, https://doi.org/10.1175/JAS-D-13-0261.1.

Grasso, L. D., and E. R. Hilgendorf, 2001: Observations of a severe left moving thunderstorm. *Wea. Forecasting*, **16**, 500–511, https://doi.org/10.1175/1520-0434(2001)016<0500:OOASLM>2.0.CO;2.

James, R. P., and P. M. Markowski, 2010: A numerical investigation of the effects of dry air aloft on deep convection. *Mon. Wea. Rev.*, **138**, 140–161, https://doi.org/10.1175/2009MWR3018.1.

Jiang, Q., and D. T. Dawson, 2023: The impact of surface drag on the structure and evolution of surface boundaries associated with tornadogenesis in simulated supercells. *Mon. Wea. Rev.*, **151**, 3037–3061, https://doi.org/10.1175/MWR-D-23-0050.1.

Jo, E., and S. Lasher-Trapp, 2022: Entrainment in a simulated supercell thunderstorm. Part II: The influence of vertical wind shear and general effects upon precipitation. *J. Atmos. Sci.*, **79**, 1429–1443, https://doi.org/10.1175/JAS-D-21-0289.1.

——, and ——, 2023: Entrainment in a simulated supercell thunderstorm. Part III: The influence of decreased environmental humidity and general effects upon precipitation efficiency. *J. Atmos. Sci.*, **80**, 1107–1122, https://doi.org/10.1175/JAS-D-22-0168.1.

Johnson, W. B., 1966: The "geotriptic" wind. *Bull. Amer. Meteor. Soc.*, **47**, 982, https://doi.org/10.1175/1520-0477-47.12.982.

Kain, J. S., and J. M. Fritsch, 1990: A one-dimensional entraining/detraining plume model and its application in convective parameterization. *J. Atmos. Sci.*, **47**, 2784–2802, https://doi.org/10.1175/1520-0469(1990)047<2784:AODEPM>2.0.CO;2.

Klemp, J. B., 1987: Dynamics of tornadic thunderstorms. *Annu. Rev. Fluid Mech.*, **19**, 369–402, https://doi.org/10.1146/annurev.fluid.19.1.369.

——, and R. B. Wilhelmson, 1978: Simulations of right- and left-moving storms produced through storm splitting. *J. Atmos. Sci.*, **35**, 1097–1110, https://doi.org/10.1175/1520-0469(1978)035<1097:SORALM>2.0.CO;2.

——, and M. Weisman, 1983: The dependence of convective precipitation patterns on vertical wind shear. *21st Conf. on Radar Meteorology*, Edmonton, AB, Canada, Amer. Meteor. Soc., 44–49.

——, R. B. Wilhelmson, and P. S. Ray, 1981: Observed and numerically simulated structure of a mature supercell thunderstorm. *J. Atmos. Sci.*, **38**, 1558–1580, https://doi.org/10.1175/1520-0469(1981)038<1558:OANSSO>2.0.CO;2.

Lasher-Trapp, S., E. Jo, L. R. Allen, B. N. Engelsen, and R. J. Trapp, 2021: Entrainment in a simulated supercell thunderstorm. Part I: The evolution of different entrainment mechanisms and their dilutive effects. *J. Atmos. Sci.*, **78**, 2725–2740, https://doi.org/10.1175/JAS-D-20-0223.1.

Lemon, L. R., and C. A. Doswell, 1979: Severe thunderstorm evolution and mesocyclone structure as related to tornadogenesis. *Mon. Wea. Rev.*, **107**, 1184–1197, https://doi.org/10.1175/1520-0493(1979)107<1184:STEAMS>2.0.CO;2.

Lin, Y.-L., R. D. Farley, and H. D. Orville, 1983: Bulk parameterization of the snow field in a cloud model. *J. Climate Appl. Meteor.*, **22**, 1065–1092, https://doi.org/10.1175/1520-0450(1983)022<1065:BPOTSF>2.0.CO;2.

Markowski, P. M., 2016: An idealized numerical simulation investigation of the effects of surface drag on the development of near-surface vertical vorticity in supercell thunderstorms. *J. Atmos. Sci.*, **73**, 4349–4385, https://doi.org/10.1175/JAS-D-16-0150.1.

——, 2020: What is the intrinsic predictability of tornadic supercell thunderstorms? *Mon. Wea. Rev.*, **148**, 3157–3180, https://doi.org/10.1175/MWR-D-20-0076.1.

——, 2024: A new pathway for tornadogenesis exposed by numerical simulations of supercells in turbulent environments. *J. Atmos. Sci.*, **81**, 481–518, https://doi.org/10.1175/JAS-D-23-0161.1.

——, and Y. Richardson, 2010: Basic equations and tools. *Mesoscale Meteorology in Midlatitudes*. John Wiley and Sons, 11–40, https://doi.org/10.1002/9780470682104.ch2.

——, and G. H. Bryan, 2016: LES of laminar flow in the PBL: A potential problem for convective storm simulations. *Mon. Wea. Rev.*, **144**, 1841–1850, https://doi.org/10.1175/MWR-D-15-0439.1.

McCaul, E. W., and M. L. Weisman, 2001: The sensitivity of simulated supercell structure and intensity to variations in the shapes of environmental buoyancy and shear profiles. *Mon. Wea. Rev.*, **129**, 664–687, https://doi.org/10.1175/1520-0493(2001)129<0664:TSOSSS>2.0.CO;2.

——, and C. Cohen, 2002: The impact on simulated storm structure and intensity of variations in the mixed layer and moist layer depths. *Mon. Wea. Rev.*, **130**, 1722–1748, https://doi.org/10.1175/1520-0493(2002)130<1722:TIOSSS>2.0.CO;2.

Moeng, C.-H., and J. C. Wyngaard, 1988: Spectral analysis of large-eddy simulations of the convective boundary layer. *J. Atmos. Sci.*, **45**, 3573–3587, https://doi.org/10.1175/1520-0469(1988)045<3573:SAOLES>2.0.CO;2.

Morrison, H., J. M. Peters, K. K. Chandrakar, and S. C. Sherwood, 2022: Influences of environmental relative humidity and horizontal scale of subcloud ascent on deep convective initiation. *J. Atmos. Sci.*, **79**, 337–359, https://doi.org/10.1175/JAS-D-21-0056.1.

Moser, D. H., and S. Lasher-Trapp, 2017: The influence of successive thermals on entrainment and dilution in a simulated cumulus congestus. *J. Atmos. Sci.*, **74**, 375–392, https://doi.org/10.1175/JAS-D-16-0144.1.

Parker, M. D., 2014: Composite VORTEX2 supercell environments from near-storm soundings. *Mon. Wea. Rev.*, **142**, 508–529, https://doi.org/10.1175/MWR-D-13-00167.1.

Peters, J. M., C. J. Nowotarski, and G. L. Mullendore, 2020: Are supercells resistant to entrainment because of their rotation? *J. Atmos. Sci.*, **77**, 1475–1495, https://doi.org/10.1175/JAS-D-19-0316.1.

——, H. Morrison, T. C. Nelson, J. N. Marquis, J. P. Mulholland, and C. J. Nowotarski, 2022a: The influence of shear on deep

convection initiation. Part I: Theory. *J. Atmos. Sci.*, **79**, 1669–1690, https://doi.org/10.1175/JAS-D-21-0145.1.

——, ——, ——, ——, ——, and ——, 2022b: The influence of shear on deep convection initiation. Part II: Simulations. *J. Atmos. Sci.*, **79**, 1691–1711, https://doi.org/10.1175/JAS-D-21-0144.1.

Ray, P. S., B. C. Johnson, K. W. Johnson, J. S. Bradberry, J. J. Stephens, K. K. Wagner, R. B. Wilhelmson, and J. B. Klemp, 1981: The morphology of several tornadic storms on 20 May 1977. *J. Atmos. Sci.*, **38**, 1643–1663, https://doi.org/10.1175/1520-0469(1981)038<1643:TMOSTS>2.0.CO;2.

Raymond, D. J., and A. M. Blyth, 1986: A stochastic mixing model for nonprecipitating cumulus clouds. *J. Atmos. Sci.*, **43**, 2708–2718, https://doi.org/10.1175/1520-0469(1986)043<2708:ASMMFN>2.0.CO;2.

Roberts, B., and M. Xue, 2017: The role of surface drag in mesocyclone intensification leading to tornadogenesis within an idealized supercell simulation. *J. Atmos. Sci.*, **74**, 3055–3077, https://doi.org/10.1175/JAS-D-16-0364.1.

——, ——, A. D. Schenkman, and D. T. Dawson, 2016: The role of surface drag in tornadogenesis within an idealized supercell simulation. *J. Atmos. Sci.*, **73**, 3371–3395, https://doi.org/10.1175/JAS-D-15-0332.1.

——, ——, and D. T. Dawson, 2020: The effect of surface drag strength on mesocyclone intensification and tornadogenesis in idealized supercell simulations. *J. Atmos. Sci.*, **77**, 1699–1721, https://doi.org/10.1175/JAS-D-19-0109.1.

Romps, D. M., 2010: A direct measure of entrainment. *J. Atmos. Sci.*, **67**, 1908–1927, https://doi.org/10.1175/2010JAS3371.1.

Rotunno, R., 1981: On the evolution of thunderstorm rotation. *Mon. Wea. Rev.*, **109**, 577–586, https://doi.org/10.1175/1520-0493(1981)109<0577:OTEOTR>2.0.CO;2.

——, and J. B. Klemp, 1982: The influence of the shear-induced pressure gradient on thunderstorm motion. *Mon. Wea. Rev.*, **110**, 136–151, https://doi.org/10.1175/1520-0493(1982)110<0136:TIOTSI>2.0.CO;2.

——, ——, and M. L. Weisman, 1988: A theory for strong, long-lived squall lines. *J. Atmos. Sci.*, **45**, 463–485, https://doi.org/10.1175/1520-0469(1988)045<0463:ATFSLL>2.0.CO;2.

Savre, J., 2022: What controls local entrainment and detrainment rates in simulated shallow convection? *J. Atmos. Sci.*, **79**, 3065–3082, https://doi.org/10.1175/JAS-D-21-0341.1.

Schenkman, A. D., M. Xue, and M. Hu, 2014: Tornadogenesis in a high-resolution simulation of the 8 May 2003 Oklahoma City supercell. *J. Atmos. Sci.*, **71**, 130–154, https://doi.org/10.1175/JAS-D-13-073.1.

Tao, T., and T. Tamura, 2020: Numerical study of the 6 May 2012 Tsukuba supercell tornado: Vorticity sources responsible for tornadogenesis. *Mon. Wea. Rev.*, **148**, 1205–1228, https://doi.org/10.1175/MWR-D-19-0095.1.

Thompson, R. L., R. Edwards, J. A. Hart, K. L. Elmore, and P. Markowski, 2003: Close proximity soundings within supercell environments obtained from the Rapid Update Cycle. *Wea. Forecasting*, **18**, 1243–1261, https://doi.org/10.1175/1520-0434(2003)018<1243:CPSWSE>2.0.CO;2.

——, ——, and C. M. Mead, 2004: An update to the supercell composite and significant tornado parameters. *22nd Conf. on Severe Local Storms*, Hyannis, MA, Amer. Meteor. Soc., P8.1, https://ams.confex.com/ams/11aram22sls/techprogram/paper_82100.htm.

——, B. T. Smith, J. S. Grams, A. R. Dean, and C. Broyles, 2012: Convective modes for significant severe thunderstorms in the contiguous United States. Part II: Supercell and QLCS tornado environments. *Wea. Forecasting*, **27**, 1136–1154, https://doi.org/10.1175/WAF-D-11-00116.1.

Weisman, M. L., 1992: The role of convectively generated rear-inflow jets in the evolution of long-lived mesoconvective systems. *J. Atmos. Sci.*, **49**, 1826–1847, https://doi.org/10.1175/1520-0469(1992)049<1826:TROCGR>2.0.CO;2.

——, and J. B. Klemp, 1982: The dependence of numerically simulated convective storms on vertical wind shear and buoyancy. *Mon. Wea. Rev.*, **110**, 504–520, https://doi.org/10.1175/1520-0493(1982)110<0504:TDONSC>2.0.CO;2.

——, and ——, 1984: The structure and classification of numerically simulated convective stormsin directionally varying wind shears. *Mon. Wea. Rev.*, **112**, 2479–2498, https://doi.org/10.1175/1520-0493(1984)112<2479:TSACON>2.0.CO;2.

——, and ——, 1986: Characteristics of isolated convective storms. *Mesoscale Meteorology and Forecasting*, P. S. Ray, Ed., Amer. Meteor. Soc., 331–358, https://doi.org/10.1007/978-1-935704-20-1_15.

——, and R. Rotunno, 2000: The use of vertical wind shear versus helicity in interpreting supercell dynamics. *J. Atmos. Sci.*, **57**, 1452–1472, https://doi.org/10.1175/1520-0469(2000)057<1452:TUOVWS>2.0.CO;2.

Xue, M., K. K. Droegemeier, and V. Wong, 2000: The Advanced Regional Prediction System (ARPS)—A multi-scale nonhydrostatic atmospheric simulation and prediction model. Part I: Model dynamics and verification. *Meteor. Atmos. Phys.*, **75**, 161–193, https://doi.org/10.1007/s007030070003.

——, and Coauthors, 2001: The Advanced Regional Prediction System (ARPS)—A multi-scale nonhydrostatic atmospheric simulation and prediction tool. Part II: Model physics and applications. *Meteor. Atmos. Phys.*, **76**, 143–165, https://doi.org/10.1007/s007030170027.

Yokota, S., H. Niino, H. Seko, M. Kunii, and H. Yamauchi, 2018: Important factors for tornadogenesis as revealed by high-resolution ensemble forecasts of the Tsukuba supercell tornado of 6 May 2012 in Japan. *Mon. Wea. Rev.*, **146**, 1109–1132, https://doi.org/10.1175/MWR-D-17-0254.1.

Zhang, C., M. Xue, K. Zhu, and X. Yu, 2023: Climatology of significant tornadoes within China and comparison of tornado environments between the United States and China. *Mon. Wea. Rev.*, **151**, 465–484, https://doi.org/10.1175/MWR-D-22-0070.1.

Zhang, R., M. Xue, and X. Yu, 2025: Environments of tornadic and non-tornadic supercells in China and optimized significant tornado parameter for China region. *Quart. J. Roy. Meteor. Soc.*, **151**, e5027, https://doi.org/10.1002/qj.5027.

Zhou, R., Z. Meng, and L. Bai, 2022: Differences in tornado activities and key tornadic environments between China and the United States. *Int. J. Climatol.*, **42**, 367–384, https://doi.org/10.1002/joc.7248.